CONTROLLED SOLIDIFICATION

OF

EUTECTIC CAST IRON

CONTROLLED SOLIDIFICATION
OF
EUTECTIC CAST IRON

By

ROBERT JOHN BRIGHAM, B.Sc., M.Sc.

A Thesis

Submitted to the Faculty of Graduate Studies

in Partial Fulfilment of the Requirements

for the Degree

Doctor of Philosophy

McMaster University

May 1966

DOCTOR OF PHILOSOPHY (1966)
(Metallurgy)

McMASTER UNIVERSITY
Hamilton, Ontario.

TITLE: Controlled Solidification of Eutectic Cast Iron

AUTHOR: Robert John Brigham, B.Sc. (McMaster University)
M.Sc. (McMaster University)

SUPERVISORS: Professors J.S. Kirkaldy and G.R. Purdy

NUMBER OF PAGES: ix, 82

SCOPE AND CONTENTS:

Eutectic Fe-C, Ni-C and Fe-C-Si alloys have been solidified directionally in an electron-beam floating zone apparatus under carefully controlled conditions and the resulting morphologies in these alloy systems have been studied as a function of rate. In addition, the transition from the stable iron-graphite (grey iron) to the metastable iron-iron carbide (white iron) mode has been observed and has been related to the iron-carbon/iron-iron carbide double phase diagram by means of undercooling measurements. Interlamellar spacing measurements carried out on both the graphitic and carbidic modes using material of the same composition and purity under identical experimental conditions showed a $\lambda \alpha R^{-1/2}$ and a $\lambda \alpha R^{-1/3}$ relationship in the iron-graphite and iron-iron carbide eutectic systems, respectively.

ACKNOWLEDGMENTS

The author is indebted to his supervisors, Dr. J. S. Kirkaldy and Dr. G. R. Purdy, for suggesting the problem and for their continuing guidance throughout the course of the work. The financial assistance of the National Research Council of Canada and the Ontario Government (in the form of graduate studentships) and of the American Iron and Steel Institute and Canada Iron Foundries, (in the form of research grants to Dr. Kirkaldy) is gratefully acknowledged.

The author wishes to thank the staff and graduate students of the McMaster Metallurgy Department for their help and stimulating discussions. In particular, thanks are due to Mr. H. Walker for his assistance in electron microscopy; to Mr. H. Neumayer for chemical analyses; and to Mr. J. H. Kelly of the Steel Company of Canada for spectochemical analyses.

TABLE OF CONTENTS

LIST OF TABLES*

---

* Tables have been placed at the end of thesis.

LIST OF ILLUSTRATIONS*

---

* Illustrations have been placed at the end of thesis.

CHAPTER 1

INTRODUCTION

Although eutectic solidification has been studied for many years with a view to clarifying commercial processes, it is only in the last decade or so that basic scientific principles have been brought to bear on the subject. This is especially true for the iron-carbon eutectic in the cast iron alloy system, where the emphasis has always been on technology.

Early literature on eutectic solidification is extensive but is mainly empirical in nature. Although the microstructure differs from system to system, certain morphological patterns are repeated. Early classification of eutectics was therefore based on morphology. This mode of classification was a worthwhile preliminary step. However, the lack of high purity materials and close experimental control invalidated most such observations as material for theoretical analysis. Again, this is especially true of cast iron metallurgy in which economics dictate commercial purities and solidification conditions have been established empirically.

The research project outlined in this thesis has been designed to clarify the eutectic solidification process in cast iron. Eutectic iron-carbon alloys of high purity have been solidified under carefully controlled conditions over a wide range of rates. The experimental apparatus, an electron-beam floating zone unit, has been chosen to minimize sample contamination and to provide sufficient flexibility in growth conditions that both the stable iron-graphite and metastable iron-iron carbide systems can be investigated.

The stable to metastable transition and the morphologies in both of these systems and in ternary and quaternary modifications have been investigated and related to the constitution diagrams.

CHAPTER 2

EUTECTIC SOLIDIFICATION

2.1 Introduction

The eutectic reaction consists of the decomposition of a liquid phase, L, to produce two solid phases, α and β, at or near the eutectic temperature, T_E, as indicated in the schematic eutectic phase diagram of Fig. 1. The spatial arrangement of the two solid phases can vary greatly so that metallographic observations of binary eutectic alloys exhibit a very wide variety of microstructures. One widely accepted classification designates eutectic structures as (i) continuous or (ii) discontinuous.

Continuous eutectics are said to occur when both phases can be traced along some unbroken path from the beginning of the solidification process to its completion. This continuity in the growth direction is characteristic of lamellar and rod-like eutectic structures. After the initial nucleation event, growth of both product phases continues at the solid-liquid interface.

Discontinuous eutectics occur when one of the phases is dispersed in the second phase as discrete particles and there is no continuity in any direction. Nucleation of the discontinuous phase at and ahead of the solid-liquid interface plays an important part in the formation of these structures. Outstanding examples are the acicular Aℓ-Si and nodular Fe-C eutectics.

2.2 Lamellar Eutectics: Theoretical

2.2.1 Introduction

In high purity eutectic alloys solidified over a wide range of conditions, a lamellar eutectic array similar to the schematic phase model of Fig. 2 is usually formed. Both isothermal transformations and controlled transformations in a temperature gradient can be treated with the same theory if it is assumed in the latter case that the interface is isothermal. Originally developed for the isothermal pearlite reaction by Zener(7) using dimensional analysis and later calculated more precisely by Hillert(2), this so-called Zener-Hillert theory provides the basis for the current theoretical interpretations of lamellar eutectic growth.

2.2.2 The Zener-Hillert Analysis

During the steady growth of a lamellar eutectic array depicted in Fig. 2, solute (B) atoms must be transported from the edge of each α lamella to the edges of the neighbouring β lamellae and this diffusion is assumed to go only through the liquid phase. If the liquid-α and liquid-β interfaces were planar, the concentration difference which provides the driving force for diffusion would be $C_L^\alpha - C_L^\beta$, where C_L^α and C_L^β denote the equilibrium concentrations according to the phase diagram of Fig. 1 of liquid in contact with α and β phases, respectively. This concentration difference will be decreased by the effect of capillarity due to the α-β boundaries. The mean pressure acting on the product phases is $2\sigma_{\alpha\beta}/\lambda$ where $\sigma_{\alpha\beta}$ is the phase boundary energy per unit area and λ is the interlamellar spacing. The Gibbs-Thomson formula suggests a correction to the concentration difference proportional to this mean pressure such that the concentration difference for diffusion will be of the form

$$(C_L^\alpha - C_L^\beta)\left(1 - \frac{\lambda_c}{\lambda}\right) \qquad (1)$$

where λ_c is a constant representing the critical lamellar spacing for zero concentration difference. Zener(7) has suggested that the effective diffusion distance is proportional to λ_β and the proportionality constant a is close to 1. Therefore

$$J = -D\frac{dC}{dx} = \frac{1}{a} D\frac{(C_L^\alpha - C_L^\beta)}{\lambda_\beta}\left(1 - \frac{\lambda_c}{\lambda}\right) . \qquad (2)$$

The mass balance requires that this lateral flux be equal to the accumulation by the β lamellae growing at a steady rate R so that

$$J = -R(C^\beta - C_E) . \qquad (3)$$

Assuming the achievement of equilibrium amounts behind the interface and no volume change accompanying the reaction, the lever rule gives

$$\lambda_\alpha(C_E - C^\alpha) = \lambda_\beta(C^\beta - C_E) = \frac{\lambda_\beta\lambda_\alpha}{\lambda}(C^\beta - C^\alpha). \qquad (4)$$

Combination of (2), (3) and (4) yields

$$\frac{R}{D} = \frac{1}{a}\frac{\lambda^2}{\lambda_\alpha\lambda_\beta} \cdot \frac{(C_L^\alpha - C_L^\beta)}{(C^\beta - C^\alpha)}\frac{1}{\lambda}\left(1 - \frac{\lambda_c}{\lambda}\right) . \qquad (5)$$

Hillert(2) has obtained essentially the same result as Zener's(7) given above by a more precise calculation.

Tiller(1) has observed that the undercooling, ΔT, is related to the slopes of the solubility lines, m_α and m_β, and the concentration difference by

$$C_L^\alpha - C_L^\beta = \Delta T \left(\frac{1}{m_\beta} - \frac{1}{m_\alpha}\right) . \tag{6}$$

Equation (5) can therefore be rewritten

$$\frac{R}{D} = \frac{1}{a} D \frac{\lambda^2}{\lambda_\beta \lambda_\alpha} \frac{\Delta T\left(\frac{1}{m_\beta} - \frac{1}{m_\alpha}\right)}{(C^\beta - C^\alpha)} \frac{1}{\lambda} \left(1 - \frac{\lambda_c}{\lambda}\right) = \beta \Delta T \ \frac{1}{\lambda} \left(1 - \frac{\lambda_c}{\lambda}\right) \tag{7}$$

to relate R, ΔT, and λ. It is clear from this that the diffusion analysis does not uniquely specify the growth rate and the spacing but yields only a relationship between them. To uniquely define the stable state, a suitable stability criterion must be determined.

Zener(7) postulated for the pearlite reaction that the growth rate is maximized with respect to variations in spacing at constant undercooling. Differentiation of (5) leads to the optimum

$$\lambda = 2\lambda_c \tag{8}$$

which in combination with (5) uniquely determines the system. This result is at least qualitatively in agreement with the experimental observations for the isothermal pearlite reaction(7).

For controlled eutectic solidification in a temperature gradient for which the undercooling and spacing vary at constant growth rate, a different stability criterion must be postulated. This will be discussed in the following sections.

The shape of the interface between austenite and pearlite as calculated by Hillert(2) is shown in Fig. 2. Analysis by electric analogue by Jackson et al(3) has indicated a similar shape for the solid-liquid interface in eutectic systems.

2.2.3 Tiller's Analysis and Postulate(1)

Tiller(1) has re-derived equation (7) by noting that the undercooling at the interface is attributable to two effects:

(1) solute pile-up during steady-state diffusion in the liquid ahead of the interface and

(2) capillarity due to the incorporation of α-β phase boundaries in the solid.

For the eutectic system shown in Fig. 1 we first calculate the first term in the undercooling ΔT. The concentration of solute in the liquid in contact with the α and β phases will be C_L^α and C_L^β, respectively, and at the α-β boundary the concentration will be C_E. For a system growing at a steady rate, R, the amount of solute rejected from the tip of an α lamella per unit area is $R(C_E - C_\alpha)$. Of this material, $R/2(C_E - C_\alpha)$ will diffuse laterally in each direction on the gradient $(C_L^\alpha - C_L^\beta)/(\lambda/2)$ where λ is the interlamellar spacing. Thus the lateral flux J is

$$J = D(C_L^\alpha - C_L^\beta)/(\frac{\lambda}{2}) = \frac{R}{2}(C_E - C_\alpha) \qquad (9)$$

From the geometry of the phase diagram (assuming straight solubility lines)

$$\Delta T = -m_\alpha (C_L^\alpha - C_E) = m_\beta (C_E - C_L^\beta) \qquad (10)$$

and

$$C_L^\alpha - C_L^\beta = \Delta T \left\{\frac{1}{m_\beta} - \frac{1}{m_\alpha}\right\} , \qquad (6)$$

where m_α and m_β are the slopes of the phase boundaries. Substitution of Equation (6) into Equation (9) gives

$$\Delta T = \frac{\frac{R}{4D}(C_E - C_\alpha)\lambda}{\{\frac{1}{m_\beta} - \frac{1}{m_\alpha}\}} \quad . \tag{11}$$

Equation (11) can be rewritten and generalized to

$$\Delta T = \frac{\frac{R\lambda}{4D}(1 - k_\alpha)C_E\,\gamma}{\{\frac{1}{m_\beta} - \frac{1}{m_\alpha}\}} \tag{12}$$

where $k_\alpha = C_\alpha/C_E$ by definition and γ is a correction factor due to the fact that one phase in general will be leading the other. Tiller has estimated $\frac{1}{2} < \gamma < 2$. Because of the approximate nature of the diffusion analysis, ΔT can at best represent an average undercooling over the interface.

An additional undercooling of the liquid is required to balance the energy increase in the solid due to α-β interfaces. When unit volume of eutectic liquid solidifies at a constant rate to a lamellar solid of spacing λ, the total α-β phase boundary produced is $\frac{2}{\lambda}$ assuming no volume change on solidification. If $\sigma_{\alpha\beta}$ is the energy of the boundary per unit area, the Gibb's free energy of the boundary is

$$\Delta F = 2\sigma_{\alpha\beta}/\lambda \tag{13}$$

To provide the energy ΔF, the eutectic liquid must be undercooled below T_E by an amount ΔT_B. The free energy change per unit volume of liquid due to this undercooling is

$$\Delta F = \frac{\Delta T_B}{T_E} \quad \rho L \tag{14}$$

where L is the latent heat of fusion per unit mass and ρ is the density of the liquid. Equating (13) and (14) gives

$$\Delta T_B = 2\sigma_{\alpha\beta} T_E / L\rho\lambda \quad . \tag{15}$$

The total average undercooling is therefore the sum of ΔT_B and ΔT. To remove the degree of freedom associated with the non-uniqueness of the expression relating undercooling and spacing, Tiller has invoked the criterion that the undercooling should be minimized with respect to spacing. This yields the expression

$$\lambda^2 R = \frac{8\sigma_{\alpha\beta}\, T_E D\{\frac{1}{m_\beta} - \frac{1}{m_\alpha}\}}{L\rho\,(1 - k_\alpha)C_E} = \text{constant} \tag{16}$$

In nearly all eutectic systems studied to date the functional dependence of Equation (16) has been verified and the order of magnitude of the derived constant appears to be right. A summary of recent results is given in Fig. 6. Recently, Tiller(4) has generalized Equation (16) by considering molecular attachment kinetics to give

$$\lambda = \text{const.}\ R^{-n} \tag{17}$$

where $n \lesssim 0.5$.

Although this analysis shows satisfactory agreement with experiment, some theoretical weaknesses must be recognized. Firstly the diffusion analysis is crudely approximate and secondly the choice of minimum undercooling as a stability criterion appears arbitrary.

2.2.4 Jackson and Chalmers' Analysis

The analysis of Jackson and Chalmers$^{(5)}$ is an attempt to circumvent the arbitrary character of Tiller's variational analysis mentioned above. It is claimed that the necessity for use of an extremum principle has been avoided by studying the behaviour of terminations of the lamellae (see Fig. 4). The assumptions implicit in this analysis are an isothermal solid-liquid interface whose undercooling is composed of two separate undercoolings, one due to the curvature of the interface, and the other due to the diffusion field ahead of the interface and a rather idealized growth morphology. The analysis consists of calculating the undercooling where a termination intersects the solid-liquid interface and at a position away from the termination in a region of perfect lamellarity. Equating the two provides a second relation between undercooling and spacing so the latter are uniquely determined.

Consider the cross section of the lamellar array normal to the interface boundary shown in Fig. 3. Resolving the surface tensions vertically, we obtain

$$2\sigma_{\alpha L} \cos \frac{\theta}{2} = \sigma_{\alpha\beta} \; . \qquad (18)$$

Also, from the geometry

$$\frac{\lambda}{4} = r \cos \frac{\theta}{2} \; , \qquad (19)$$

and therefore

$$\cos \frac{\theta}{2} = \frac{\sigma_{\alpha\beta}}{2\sigma_{\alpha L}} = \frac{\lambda}{4r} \; , \qquad (20)$$

or

$$\frac{\sigma_{\alpha L}}{r} = \frac{2\sigma_{\alpha\beta}}{\lambda} \quad . \tag{21}$$

The undercooling due to steady-state diffusion in the liquid ahead of the interface was calculated in the Tiller analysis and given in Equation (12). Because of the idealized case chosen where $m_\alpha = -m_\beta$ and neither phase is leading, Equation (12) can be written

$$\Delta T = \frac{R\lambda}{4D}(1 - k_\alpha)\, C_E\, m_\alpha \quad . \tag{22}$$

From the Gibbs-Thomson formula, the undercooling at the centre of a lamella of curvature r is given approximately by

$$\Delta T_r = \sigma_{\alpha L} \frac{T_E}{Lr} \quad . \tag{23}$$

Substituting from Equation (21) gives

$$\Delta T_r = \frac{2\sigma_{\alpha\beta}\, T_E}{L\lambda} \quad . \tag{24}$$

In addition, ΔT_c and ΔT_r can be calculated at the position of a termination shown schematically in Fig. 4. The termination has curvature in two directions so

$$\Delta T_r = \frac{4\sigma_{\alpha\beta}\, T_E}{L\lambda} \quad . \tag{25}$$

The amount of solute rejected by the half-cylinder of the termination per unit time is

$$(1 - k_\alpha)\, C_E\, R\, \frac{\pi}{2}\, \frac{\lambda^2}{16} \tag{26}$$

which diffuses to the continuous β phase across the semi-circular interphase boundary. The diffusion equation is

$$(1-k_\alpha)\ C_E\ R\,\frac{\pi}{2}\ \frac{\lambda^2}{16} = D\,\frac{(C_L^\alpha - C_E)}{\frac{\lambda}{4}} \cdot \frac{\lambda}{2} \cdot \pi \cdot \frac{\lambda}{4} \qquad (27)$$

or

$$(C_L^\alpha - C_E) = \frac{(1-k_\alpha)\ C_E\ R\ \lambda}{16\ D} \qquad (28)$$

giving

$$\Delta T = \frac{m_\alpha\ (1-k_\alpha)\ C_E\ R\ \lambda}{16\ D}\,. \qquad (29)$$

On the assumption of an isothermal interface, the sum of Equations (22) and (24) can be equated with the sum of Equation (25) and (29) to give

$$\lambda^2 R = \frac{32\sigma_{\alpha\beta}\ T_E\ D}{m_\alpha\ (1-k_\alpha)\ C_E\ \lambda} = \text{constant} \qquad (30)$$

This relationship differs from Tiller's result by only a constant.

Jackson and Chalmers' claim that they have succeeded in obtaining the experimentally observed relationship without any arbitrary extremum principle is open to question. Actually, they have done nothing more than conceal the principle within their assumption of an isothermal interface. They are saying, in effect, that in a directional heat flow system, nature abhors lateral gradients which may be a corollary of a dissipation principle.

2.2.5 Stability Criteria

In this section, a brief outline of the need for stability criteria will be given. No attempt will be made to critically review this area of theoretical interest and only a few contributions related directly to eutectic solidification will be referenced.

In the previous sections, the three variables characteristic of lamellar eutectic solidification have been mentioned. These are the lamellar spacing, λ, the undercooling at the interface, ΔT, and the rate of solidification, R. In most, and indeed in this investigation of eutectic solidification, the rate, R, is fixed at some steady value by the experimental procedure. However, the other variables, λ and ΔT, cannot be fixed experimentally and are related by diffusion theory by a single relation only (see Equation 7). The remaining degree of freedom necessitates a further relation between λ and ΔT to uniquely determine the system at constant R. A possible source of such a relation may be found in a variational principle which defines the stability of a heterogeneous steady state system.

For example, in Section 2.2.3, Tiller(1) chose minimum undercooling and in Section 2.2.2, Zener(7) chose maximum growth rate as the stability criterion. However, these choices are arbitrary. More fundamental and universally acceptable principles may be found in the thermodynamics of irreversible processes(10).

The principle of minimum entropy production has been applied to eutectic solidification by Tiller(8) and by Li and Weart(9). Tiller(8) finds that this is equivalent to minimum undercooling for a broad range of experimental parameters. Kirkaldy(96), on the other hand, finds that the experimentally observed relations for both isothermal and controlled eutectics can be derived from a principle of maximum entropy production. Opinion on the validity of these calculations still remains divided so that the question must be regarded as open.

2.3 Lamellar Eutectics: Experimental

The relationship

$$\lambda \alpha R^{-\frac{1}{2}} \tag{16}$$

which was first developed by Tiller(1), has been observed in most pure eutectic alloys to within experimental error. This may be regarded as empirical evidence in favour of the principle of minimum undercooling. In his investigation of the Aℓ-Mg eutectic, Yue(6) has shown that the temperature gradient in the liquid has no observable effect on this relationship. The $R^{-1/2}$ law is found for Pb-Cd(70), Pb-Sn(70), Aℓ-Zn(70), $CuA\ell_2$-Aℓ(70), Zn-Sn(71), Aℓ-Mg(6), and Cd-Zn(71) as shown in Figure 5 which was taken from Tiller(72). In addition to these results for low temperature eutectics, Lakeland(37) has confirmed the $R^{-1/2}$ relationship for the Fe-C, Ni-C, and Fe-C-Si eutectic systems for which the eutectic temperature exceeds 1000°C.

However, the results of Wilkinson and Hellawell(26) in the $Fe\text{-}Fe_3C$ system indicate an $R^{-1/3}$ relationship. Furthermore, Cooksey et al(92) have reported values of the exponent, n, in Equation (18) equal to 0.36, 0.35, and 0.40 for the Aℓ-Zn, Ag-Cu, and Mg-Aℓ eutectics, respectively. Whelan(73) has attributed these deviations from the $R^{-1/2}$ law to convective effects on the transport of solute. A critical experiment involving the solidification of both the Fe-C and the $Fe\text{-}Fe_3C$ eutectic systems of the same composition in the same apparatus will be discussed in this thesis.

In the Tiller analysis, the combination of Equation (16) and the sum of Equation (12) and Equation (15) leads to the relation

$$\Delta T \alpha R^{\frac{1}{2}} \tag{31}$$

where ΔT is the undercooling at the interface with respect to the equilibrium eutectic temperature. Recently Hunt and Chilton(74) have observed such a relationship for the Pb-Sn eutectic system although the growth conditions in their experiment were not strictly steady-state.

2.4 Continuous Modified Eutectics

In discussing modified eutectics, the classification due to Chadwick(5) will be followed. The term "modified eutectic" will be used to describe any change in structure from the regular lamellar which arises from the presence of small amounts of impurities. This classification includes the commonly observed colony and rod-like structures.

The colony structure observed by Weart and Mack(11) and the accompanying cellular (non-planar) interface is analogous to the cellular structure in single-phase binary alloys(12). In the eutectic, when an impurity element is rejected by both growing phases, a constitutionally supercooled region is built up ahead of the interface. The plane interface is no longer stable since any perturbation will tend to grow to relieve the supercooling. In the steady-state, a colony structure results in which the impurity is rejected to the cell boundaries on a macroscopic scale. The morphology within each cell remains lamellar.

When the distribution coefficients of the impurity element in the eutectic phases are sufficiently different, the lamellar structure can become unstable and be replaced by a rod-type structure. Chadwick(5) has explained this lamellar to rod modification on the basis of short-range constitutional supercooling in which one phase grows into the constitutionally supercooled liquid ahead of the other, and the lamellae of the lagging phase break up into very small cells surrounded by the other phase. Yue(13) has observed the lamellar to rod transition in the Aℓ-Mg eutectic system as the impurity content is increased.

An intermediate structure can also develop in impure eutectic alloys growing with a cellular interface. This structure consists of a regular lamellar morphology at the centre of cells but a rod-like morphology at the cell boundaries. Such a structure can be rationalized if the distribution coefficients of the impurity element in the eutectic phases are equal at low impurity concentrations as at the cell tips but different at higher concentrations corresponding to the cell boundaries. The explanation of Chadwick(5) outlined above then applies.

2.5 Discontinuous Eutectics

In the lamellar type of eutectic and in its modified forms, each phase grows continuously so that repeated nucleation is not required. A discontinuous eutectic is one in which one of the phases must renucleate repeatedly due to the termination of growth of crystals of that phase. A typical discontinuous eutectic is the Aℓ-Si eutectic in which individual crystals of Si are dispersed in an Aℓ matrix. The Fe-C discontinuous eutectic, nodular cast iron, has many similarities to the Aℓ-Si eutectic.

Recent reviews by Bell(14) and Chadwick(5) have elucidated the formation of the Aℓ-Si discontinuous eutectic which forms under conditions of high growth rate or modification with small amounts of Na. The analogous modification of the Fe-C eutectic will be discussed in Chapter 4 in a review of cast iron literature.

2.6 Summary

The classification of eutectic morphologies as either continuous or discontinuous has been chosen because of its simplicity and its lack of ambiguity, particularly in the iron-carbon eutectic systems. Scheil's(75) classification into normal, anomalous, and degenerate eutectics exhibiting simultaneous growth, less coupled growth, and no coupling between the two phases, respectively, is much more ambiguous.

Current theories of lamellar eutectic growth have been outlined and have been compared with experimental findings. Since only the most idealized growth models can be treated analytically, contributions to the theory of modified and discontinuous eutectics remain descriptive. For this reason, a discussion of nodular cast iron will take the form of a literature review.

CHAPTER 3

THE IRON-CARBON PHASE DIAGRAM

3.1 Introduction

The stable iron-graphite phase diagram which is necessary for an understanding of the solidification of cast iron is well known in the eutectic range. The 1948 compilation due mainly to Mehl and Wells(15) has been modified and brought up to date by Hansen(16). A more recent revision has been carried out by Kirkaldy and Purdy(17). This later modification is confined mainly to the eutectoid region and differs only slightly from the Hansen version in the eutectic area. The metastable Fe-Fe_3C system is also well established except for the liquid -Fe_3C solubility line. This is indicated by full lines in Fig. 6 after Kirkaldy and Purdy(17).

3.2 Thermodynamics of Iron-Carbon Alloys

The phase diagram of Figure 6 represents the equilibrium phase relationships. For systems removed from equilibrium, such as during solidification, knowledge of the metastable boundaries at temperatures below the eutectic is desirable. Hillert(18) has facilitated the extrapolation of the stable boundaries to lower temperatures by fitting analytical expressions. In the liquid phase, he has represented the activity coefficient, γ, by a series expansion

$$\ln \gamma_c = K + ax_c + bx_c^2 \tag{32}$$

where x_c is the concentration of carbon expressed in atom fraction. The temperature dependence, K, is accounted for by the empirical relation

$$K = \frac{A}{T} + B \tag{33}$$

In the austenite phase the following expansion was chosen,

$$\ln \gamma_c = K - \frac{1}{2} a \ln (1 - 2x_c) \tag{34}$$

where K has the same temperature dependence as for the liquid.

By fitting the equations to several well defined experimental points, Hillert$^{(18)}$ was able to summarize the thermodynamics in the eutectic region in four equations. Based on standard states of pure liquid iron and pure graphite, the results are:

$$\ln a_c = \ln x_c - 3.5 \ln (1-2x_c) - 2.0968 + \frac{5405.4}{T} \tag{35}$$

$$\ln a_c^L = \ln x_c^L + 17.702\, x_c^L - 34.173\, (x_c^L)^2 - 1.8977 + \frac{2333.0}{T} \tag{36}$$

$$\ln a_{Fe} = -6 \ln(1-x_c) + 3.5 \ln(1-2x_c) - 7.5524 + \ln T + \frac{101.4}{T} \tag{37}$$

$$\ln a_{Fe} = - 49.644 \ln (1-x_c^L) - 50.644\, x_c^L - 34.173\, (x_c^L)^2 \tag{38}$$

where $a = \gamma x_c$ represents the thermodynamic activity of the species denoted in the subscipt. The superscript, L, indicates the liquid phase. From Equation (35) to (38) and the thermodynamics of cementite (Fe_3C) tabulated by Darken and Gurry$^{(19)}$, the equilibrium lines in the eutectic region have been calculated(21). Figure 7 shows the result. The dashed lines represent the metastable system while all the thick lines, full as well as dashed, were calculated. The thin lines were taken from Hansen's(16) phase diagram and differ only slightly from the Kirkaldy and Purdy(17) compilation of Fig. 6.

Two interesting features of Fig. 7 are apparent. The melting point of Fe_3C is predicted to be 1480°K (1207°C) in contrast to published values as high as 1837°C (20). Because of the low melting point, the Fe_3C-liquid solubility line is much more horizontal than previously thought and intersects the graphite-liquid solubility line at 1415°K (1142°C), only 11°C below the temperature of the stable eutectic on the Hansen diagram. Hillert(21) made these predictions some ten years ago.

3.3 Consequences of the Double Diagram

From the iron-carbon phase diagram, it would appear that eutectic liquid, when cooled slowly (at small undercooling), would solidify to produce the stable iron-graphite product. This is certainly the case for undercoolings of less than 6°C because in this temperature range graphite is the only possible product. However, below the Fe-Fe_3C eutectic temperature, eutectic liquid is supercooled with respect to both the stable iron-graphite and metastable iron-iron carbide eutectics. In this region, Fe_3C can grow if nucleated but the eutectic liquid is more highly supersaturated with respect to graphite than carbide. At a temperature below the intersection of the graphite-liquid solubility lines, the carbide phase becomes the thermodynamically stable phase with respect to supercooled liquid. This is shown schematically in the free energy-composition diagrams of Fig. 8 which are similar to those of Hillert(76).

Fig. 8(a) shows schematically the double diagram and Fig. 8(b) - (f) indicate the free energy - composition curves at the temperatures shown. When the temperature falls below T_1, graphite can start to form but cementite cannot. At undercoolings greater than T_2, the formation of cementite is thermodynamically possible but the supersaturation with respect to graphite is greater than that with respect to cementite. Fig. 8(d) shows an intermediate temperature, T_3. The fact that the two phase boundaries intersect at T_4 reveals that, with further decrease in temperature, saturation with respect to cementite increases more than with respect to graphite. Below the intersection at T_5, cementite becomes the stable phase with respect to supercooled liquid.

In the iron carbon system, one would expect to find the stable iron-graphite eutectic at slow freezing rates. As the freezing rate increases, a transition from graphite to carbide seems probable at undercoolings greater than 11°. Furthermore, since the carbide to graphite transition relies upon a nucleation step, carbide may also be the observed phase at undercoolings between 6°C and 11° below the graphite eutectic temperature if conditions for graphite nucleation have been avoided.

3.4 Summary

From the accepted phase diagram and the thermodynamic predictions of Hillert(18, 21, 76), a transition from a graphite to carbide eutectic phase should take place in this system at an undercooling of about 11°C below the Fe-C eutectic temperature. In this investigation, an attempt will be made to observe and measure the undercooling of such a transition.

CHAPTER 4

REVIEW OF CAST IRON LITERATURE

4.1 Introduction

As observed in the previous chapter, the double eutectic diagram indicates the possibility of solidification of cast iron in two thermodynamic systems. The product is called white cast iron if carbidic and grey cast iron if graphitic. While early researchers studied cast iron mainly from a technological and industrial point of view, current interest has turned to the more fundamental aspects of cast iron solidification. The post-war review paper of Morrogh and Williams(22) is a comprehensive compilation of the early work and will therefore be taken as a base line for this review. Reviews of more recent work have been compiled by Kirkaldy(17), Chadwick(5), and Hughes(23).

4.2 White Cast Iron Solidification Structures

The formation of carbide-austenite eutectic structures has recently been studied metallographically by Rickard and Hughes(24). They have observed that white cast iron may solidify with either the well-known dendritic ledeburite structure or with a plate-like structure as shown in Fig. 9. The plate-like structure is promoted by a decreased nucleation rate such as occurs in superheated melts. The tendency of Fe_3C to form plates was also noted by Hillert and

Steinhauser(25) and the structure was studied in detail. An artist's conception of growing ledeburite eutectic cells is given in Fig. 10.

Wilkinson and Hellawell(26) have studied the carbidic eutectic solidification of pure alloys under controlled conditions. Directional solidification produced a regular lamellar eutectic structure at high solidification rates but obtained a mottled structure at rates less than 40 mm/h apparently due to spurious nucleation events at the contact between the horizontal mold and ingot. Brigham et al(27) have also reported lamellar carbide structures in pure iron-carbon alloys solidified under controlled conditions.

4.3 Grey Cast Iron Solidification Structures

Bunin et al(28) suggested that the graphite in each grey iron eutectic cell forms a continuous network which frequently branches, in contrast to the idea that each graphite flake was individually dispersed through a metallic matrix. Morrogh and Oldfield(29) have substantiated this model by deep etching techniques. Fig. 11 shows the artist's conception of a typical extracted cell(30). Oldfield(31) has presented a stereo-photograph of a deep-etched micro-specimen showing vividly the three dimensional nature of the branched graphite skeleton. The cooperative growth of the graphite and austenite to form the eutectic is now well understood(32, 33, 30).

An increase in the solidification rate or increased undercooling causes an increase in the frequency of branching and therefore a much finer structure known as lacy(34, 36) or ASTM D-type(35) graphite. In controlled solidification experiments, high purity eutectic Fe-C and Fe-C-Si alloys have been solidified at various steady rates giving graphite morphologies ranging from coarse directional flakes at slow rates to a fine lacy structure at high rates(37, 27).

Oron and Minkoff(77) have investigated graphite dendrites from the analogous Ni-C eutectic system and have determined that these are bi-crystals growing in a twinned orientation. However, the concept of flake growth by the edgewise extension of basal planes is still acceptable for at least part of the flake and the crystallographic requirements for branching in the twinned structure are greatly reduced. The internal substructure in the branched flakes could result from mechanical distortion of the leading graphite phase by convective currents in the liquid. The wavy appearance of individual flakes can be explained in a similar manner.

4.4 Grey or White Iron Solidification

4.4.1 Effect of Cooling Rate

The effect of cooling rate on the solidification of pure iron-carbon alloys was discussed above in Section 3.3. It was noted that slow cooling rates promoted grey iron solidification and rapid cooling promoted white. Quantitative measurements of the solidification temperature as a function of rate of heat extraction in commercial cast irons have been made by Oldfield(31). In that investigation, the temperature at which the Fe-C eutectic solidified decreased markedly with extraction rate while the solidification temperature of the Fe-Fe_3C eutectic remained almost invariant. Extrapolation of the two results to zero extraction rate agreed with the equilibrium melting point of both the stable and metastable systems.

Whether the stable graphite phase forms directly from the melt or indirectly by the decomposition of Fe_3C has been questioned. However, coarse flake and lacy graphite morphologies were observed in cast irons which were solidified between the stable and metastable eutectic temperature showing conclusively that these forms of graphite precipitate directly from the melt(31). Commercial cast irons therefore appear to solidify in accordance with the double diagram.

4.4.2 Effect of Alloy Additions

In the jargon of cast iron technologists, chill is said to occur when solidification of the grey iron eutectic is suppressed and white iron solidification occurs,while mottle is the term used to designate an area in which both graphite and carbide solidification structures occur. The effect of alloy additions on chill and mottle formation in cast irons has been studied extensively and has been reviewed recently by Boyes and Fuller(38).

Investigations of chill have been carried out by casting the iron into vertical sand molds approximately 1 1/8 inches wide, 5 inches long and 9 inches high standing on 1 3/4 inch steel chill blocks(32) to provide an initial rapid solidification. The depth to which chill and mottle occurred was measured by direct observation of the broken casting. Because solidification in all castings occurred under similar conditions, the chill depth is a qualitative guide to the effects of various additions.

Among the major elements found in cast iron, increasing amounts of P(40), Si(39), and carbon(38) decrease the chill depth while excess S(45), excess Mn(44), and Cr(41) increase the chill depth. Oldfield has shown that the effects of Cr(46) and Si(47) have a purely constitutional effect in changing the chill characteristics of the melt in contrast to inoculation effects which will be discussed later. As shown in Fig. 12, an increase in the Si content increases the temperature difference between the stable graphite-austenite and metastable ledeburite eutectic equilibrium temperature and the temperature range wherein only graphite can grow is expanded. Si therefore stabilizes graphite and reduces chill formation. Cr has the opposite effect and increases chill formation by decreasing the temperature difference between the stable and metastable equilibria. The partition of alloying elements between the phases has not been investigated with the exception of Cr, which segregates to the carbide phase(78).

Manganese and sulphur are elements commonly used to control chill depth but because of their reaction in the liquid state, the effects of individual elements is not clearly understood. Excess Mn(44), above that necessary to react with the S, increases chill, probably by a thermodynamic effect similar to that of Cr(46). Excess S(45) also increases chill depth but the observations of Oldfield(31) indicate a different cause of the effect. Oldfield(31) found that at a constant rate of heat extraction an increase in S content increased the amount of undercooling in the melt and consequently stabilized carbide formation. Because the nucleation characteristics of the melt were unaffected by S concentration, the increased undercooling occurred because S reduces the growth rate of each eutectic cell. The addition of Mn to high S melts initially reduces chilling by reacting with excess sulphur but an increase in Mn beyond a certain level leads to increased chill depth because of the excess Mn. The empirical relationship for a balanced iron is one in which % Mn = 1.7 x % S.

Boron(42) has proven to be one of the most powerful elements for increasing depth of chill. Addition of as small as 0.05 % B may be used to give a uniform mottled structure irrespective of section size while 0.20 % B produces predominantly white structures although some very fine mottle may be obtained.

The chill effects of most of the minor elements found in cast irons including dissolved gases have been reviewed(38).

4.4.3 Inoculation Effects

The phenomena discussed above are due to the persistent effects of alloy additions rather than to transient inoculation effects associated with last minute additions to the melt. Fuller(43) has shown, for example, that Aℓ increases the rate of nucleation of graphite and so decreases the depth of chill in test castings.

The only effect of increasing Aℓ content in the melt is an increase in the degree of nucleation whether Aℓ is added to the cold furnace or to the ladle. Lux and Tannenberger(48) and Dawson(50) have shown that commercial ferrosilicon containing Ca and Aℓ impurities acts as a strong inoculant and decreases chill depth, presumably by supplying heterogeneous nucleation sites for graphite. High purity ferrosilicon has no inoculation effect(48). Merchant et al(79) have shown that ferrosilicon inoculation is most effective in irons of low carbon content. In addition to ferrosilicon, graphite, calcium silicide, and silicon-manganese-zirconium alloys increase the degree of nucleation of the iron and consequently reduce the depth of chill(38).

Any process which destroys heterogeneous nucleation sites provided by inoculation will have the effect of increasing the chill depth. Fuller(49) has shown that the number of eutectic cells decreases with increased holding time and temperature in the furnace. Bubbling an inert gas such as nitrogen through the melt has a similar effect(38).

4.4.4 Inverse Chill and Inverse Greyness

The phenomena of inverse greyness (a grey rim on a white casting) and inverse chill (a white core in a grey casting) have been investigated by Hughes and Oldfield(51) and by Hillert(52). Hillert considers these transformations to be related phenomena and he explains them on the basis of the nucleation of carbide under the changing conditions of casting solidification. In castings exhibiting inverse chill and inverse greyness, the first product of solidification is grey iron which is nucleated at the surface. At some time during the growth process, the conditions for nucleation of white iron may become favourable in the remaining melt. Local enrichments of carbide stabilizing elements caused by macro- or microsegregation between the growing graphite eutectic cells or a local temperature decrease associated with a thin section may lead to the required conditions. Hillert(52) has shown that after cementite is nucleated, ledeburite will grow with considerable speed and spread to all the remaining melt although this may have a higher temperature or a less favourable composition. This initial grey but subsequent rapid white iron growth results in castings with carbidic centres and graphitic rims.

The investigation of Hughes and Oldfield(51) produced results which are not inconsistent with Hillert's(52) suggested mechanism. These authors have shown that the factors promoting inverse chill are high and unbalanced sulphur content, high hydrogen content and a low degree of nucleation. Limited graphite nucleation confines graphite growth to the rim of the casting and prevents general precipitation of graphite. As discussed earlier in Section 4.4.2, Boyes and Fuller(38) have shown that sulphur and hydrogen stabilize carbide and promote chill formation. The local segregation of these elements during initial grey solidification may be responsible for the observed changes in solidification mode.

4.5 Nodular Iron Solidification

4.5.1 Introduction

Prior to 1947, the spheroidal graphite morphology in cast iron had been produced only by the solid state decomposition of carbide. At that time, Morrogh(53) and Gagnebin(54) independently demonstrated that such structures could be produced in the as-cast condition, the former by the use of cerium additions and the latter by the introduction of magnesium. The mode of formation has been demonstrated by Oldfield and Humphreys(55) who observed that nodular iron formed between the carbide and graphite eutectic temperature. The mechanism by which nodular iron is formed is well known and several authors(34, 55, 56) have demonstrated by quenching from different points on the cooling curves that the eutectic grows in the manner shown schematically in Fig. 13. Nuclei appear in the liquid and the intermediate structure consists of a layer of austenite surrounding a single graphite spherulite. Growth occurs by carbon diffusion through the austenite envelope.

Polarized light microscopy(53, 57, 22) and X-ray analysis(58) have shown that the graphite spheroids are bounded by basal planes. Patterson and Ammann(80) have drawn attention to the strong anisotropy of the graphite surface free energy and have suggested that the spheroidal growth morphology is adopted to minimize the free energy of the system. The anisotropy exhibited by the surface free energy of graphite should similarly be observed in the interfacial energy between graphite and liquid or austenite. The total free energy of the system is decreased therefore by the spheroidal morphology exhibiting only low energy interfacial boundaries.

Unfortunately, the above argument is difficult to sustain simply on the basis of a lower surface free energy since the flake morphology also exhibits low energy interfacial boundaries. In addition, a large number of spheroids is necessary to accommodate the volume of a single flake so that the spheroidal morphology may not in fact minimize the total surface energy of the graphite.

4.5.2 Factors Determining Nodular Iron Formation

Bolotov et al(81) have pointed out that a spheroidal graphite morphology results after a cast iron has been treated under specific conditions with one of the following elements: Mg, Ce, Ca, Li, Bi, Na, K, Te, Se, Ba, Sr or Zn. However, Barton(82) has indicated that the only method of attaining satisfactory structures on an economic basis has been by the addition of magnesium, either as pure Mg or as one of its alloys. Magnesium in combination with cerium in the form of mischmetall has also been successfully used.

Numerous mechanisms for explaining modification by the above elements and for spheroidal growth have been offered. Loper et al(83) have summarized these as follows:

1. The modifying element alters the surface tension of the melt. The contact angle of the two solid phases in a cooperative eutectic is said to be altered in such

a way that overgrowth and isolation of one of the phases occurs.

2. Substrate nucleation. Some particle in the melt provided by the modifying element serves as a substrate for nucleation and determines the spheroidal crystal growth morphology.
3. Adsorption of modifying elements. The modifying element is adsorbed on the surface of the growing phase and thereby alters its growth kinetics and morphology.
4. The phase diagram is materially altered by the presence of very small percentages of the modifying element and the resulting phase system inherently produces a spheroidal morphology.
5. Gas bubble theory. The modified phase grows within gas bubbles generated by the modifying element.
6. Supercooling. The modified element causes substantial undercooling resulting in the spheroidal phase morphology.

None of the theories mentioned above has been able to attain universal acceptance and several can be dismissed immediately. The gas bubble theory of Gorshkov(84, 81) is one such theory. Theory 4 is also rather dubious on the basis of Scheil's(85) investigation of Na modification in the analogous Aℓ-Si system which shows that a Na concentration sufficient to produce modification depresses the eutectic temperature only a negligible amount.

As an introduction to the discussion of the mechanism of modification we note the following common feature of all the modifying agents listed above. Each of the elements has a high affinity for sulphur and forms a very stable high melting point sulphide. This is especially true of Mg and Ce which are used commercially. Other elements, such as Mn, form stable sulphides but do not lead to modification. Barton(82) has shown that the amount of Mg added to a cast iron to produce a purely nodular structure is directly proportional to its sulphur content. If the sulphur content is greater than 0.015%, 0.035 - 0.040% residual Mg in solution and in the form of sulphides is required, but if the iron contains less than 0.015% S, less Mg is required. Desulphurizing practices for cast irons(86) before the addition of expensive modifying agents are economically feasible(82, 86) for this reason.

Each of the theories, 1 through 3, mentioned above can now be discussed as a possible factor in the formation of nodular graphite. We must from the start discount 6 since although a high supercooling is a common feature of commercial melts which solidify with a spheroidal graphite morphology, this characteristic is caused by rather than being a cause of the solidification mechanism. As shown schematically in Fig. 13, the growth of the graphite spheroid relies on carbon diffusion through the thickening austenite envelope. A temperature decrease below the eutectic temperature increases the carbon gradient in the austenite layer (see the extrapolation of phase boundaries to lower temperatures in Fig. 7) and consequently increases the carbon flux to sustain the graphite precipitation reaction. A high supercooling is therefore expected since carbon must be "driven" through the austenite layer by solid state diffusion at a rate sufficient for the heat of reaction to equal the rate of heat extraction from the melt. Thus, the supercooling is associated with the solidification mechanism but is not the cause of modification.

Substrate nucleation undoubtedly plays an important role for it is a known fact that stable high melting sulphides will be present in the modified melts. These heterogeneous nuclei are very effective as shown by the much higher rate of nucleation in modified nodular melts than in melts with a flake graphite morphology(55). Lyubchenko et al(64) have observed a central nucleus of high Ce content in graphite nodules indicating nucleation on a cerium compound, possibly CeS. In commercial cast iron treated with nickel-magnesium, electron microprobe studies(93, 94) have indicated a nucleus rich in Mg and Si and electron microscopy(95) has been used to identify the compound $3MgO . 2SiO_2 . 2H_2O$. Although there is conclusive evidence that Mg and Ce compounds act as effective heterogeneous nucleation sites for graphite, these nucleation events, per se, can in no way be linked to the subsequent growth morphology.

An important role for surface tension effects in nodular iron formation has been proposed by many authors, presumably based on the theory that graphite grows with basal planes out to minimize the surface energy(80). To sustain the argument, the initial stage of graphite envelopment by austenite must be explained and must follow from the fact that graphite is the leading phase in the flake morphology.

The effect of sulphur on the surface properties of cast irons is well known. For example, Kozakevitch et al(60) have shown that increasing sulphur concentrations greatly reduce the surface tension or surface free-energy, $\sigma_{\ell g}$, of Fe-C alloys while Khranov and Chernobrovkin(62) have observed a similar change in surface properties accompanied by a decrease in contact angle of cast iron wetting graphite. A surface tension balance is given by

$$\sigma_{s\ell} = \sigma_{sg} - \sigma_{\ell g} \cos \theta$$

where $\sigma_{s\ell}$ is surface free-energy of a solid-liquid interface, σ_{sg} is the surface free-energy of a solid-gas interface and $\sigma_{\ell g}$ is the surface free-energy of a liquid-gas interface and θ is the contact angle. For a system consisting of liquid cast iron on a graphite block in a neutral atmosphere, the addition of sulphur to the cast iron should not change σ_{sg}, but $\sigma_{\ell g}$ and θ decrease as mentioned above (60, 62). The result is a decrease in $\sigma_{s\ell}$ with increasing sulphur. Therefore, the addition of Mg or Ce, which reduce the sulphur content of the melt, will cause an increase in $\sigma_{s\ell}$. This means that the graphite is not wet by a low sulphur (high Mg) melt so the possibility that austenite can overgrow and envelope any graphite nucleus that forms in the solidification process is increased and the formation of a flake morphology is suppressed. Sidorenko and Tsarevskii(61) have observed similar changes in the surface properties of the analogous Ni-C system and they have observed a change from spheroidal to flake graphite morphology with increasing sulphur content.

Modification by the adsorption of modifying elements has been proposed by Minkoff(59) based on observatins in the Ni-C system containing trace amounts of impurity. His observation of fern-like intermediate graphite morphologies led him to the conclusion that a continuing flux of impurity is necessary to maintain the spheroidal form. Adsorption of impurity atoms on selected planes which "poisons" the normally fast-growing crystal facets to produce a structure bounded by basal planes has been postulated. Autoradiography has shown that the nodularizing agent is uniformly distributed throughout the graphite spheroid(63, 64, 81) and that the sulphur content of nodules is very low compared to the enrichment of sulphur in graphite flakes(81). The screw dislocation growth mechanism of Hillert and Lindblom(64) also supports the adsorption model for modification although it is not clear to this author how a continuing flux of modifying element can be maintained through a thickening austenite envelope.

A model based on the adsorption of sulphur rather than modifying agent can explain the experimental observations. In this case, the role of the modifying agent is to control the sulphur by forming sulphides and reducing the residual sulphur content of the melt. The proposed model is outlined schematically in Fig. 38.

As indicated in Fig. 38(1), initial nucleation of graphite occurs at several points on a heterogeneous nucleating substrate with basal planes parallel to the substrate. These nuclei grow laterally until they impinge as shown in Fig. 38(2). Thickening of the graphite takes place at a repeatable step provided by a screw dislocation mechanism as proposed by Hillert and Lindblom(64).

This nucleation mechanism and primary growth stage is a common feature of both flake and nodular graphite growth.

For nodular growth, in which sulphur is well controlled by modifying agents, thickening of the graphite continues by the screw dislocation mechanism and the spheroidal morphology persists as shown in Fig. 38(3). Subsequent envelopment by austenite produces the nodular morphology of Fig. 38(4) which is indentical to that formed by the accepted growth mechanism shown in Fig. 13.

On the other hand, adsorption of sulphur on the basal plane has a cumulative effect in blocking the screw dislocation mechanism by which the graphite plates thicken. When growth inhibition occurs, graphite growth kinetics rather than carbon diffusion to the graphite will become rate controlling. Consequently, a local supersaturation of carbon at the surface will occur which is expected to lead to a non-planar interface analogous to interface instability in constitutionally supercooled alloys. The re-nucleation of graphite with a different orientation at an imperfection such as a sub-boundary can therefore be postulated. This proposed mechanism leads initially to the structure illustrated in Fig. 38(5) and finally to the true flake morphology of Fig. 38(6). Flake growth is not inhibited by sulphur because no cumulative growth blockage occurs during the edgewise extension of graphite plates.

The low sulphur content of graphite nodules as compared to the enriched sulphur concentration in flakes(81) and the intermediate fern-like morphology(59) are features which are consistent with this model. Fern-like structures which result from insufficient modifying agent additions (and poor sulphur control) can be explained on the basis of localized adsorption resulting from the transport of sulphur through ruptures in the austenite envelope. Again, local supersaturation of carbon and re-nucleation of graphite can be postulated. A continuing flux of the adsorbed element through the austenite envelope is not required to produce the spheroidal graphite morphology.

Although Minkoff(59) discounts the role of surface energy changes, Khrapov(65) considers that an increase in surface tension is a necessary but not sufficient condition for nodular growth. Of the theories for nodular growth summarized above, the first and third seem to agree most closely with experimental findings to date.

4.6 Summary

The literature in the cast iron field is extensive but to a large extent lacks a sound scientific basis. Observations of cast iron solidification have been made on complex multicomponent systems without a knowledge of the behaviour of pure Fe-C alloys for comparison. Sand castings have supplied interesting empirical results for chill and mottle formation but close experimental control over growth conditions has been lacking. This suggests that a better understanding of the process may be gained by studying a carefully controlled experimental system of precisely known composition.

CHAPTER 5

EXPERIMENTAL APPARATUS

5.1 Introduction

The central aim of this research project was to study the solidification of the pure iron-carbon eutectic under carefully controlled conditions.

Contemporary investigators have studied the cast iron systems using induction heating in a water-cooled copper boat(26) and radiative heating in a recrystallized alumina boat(37). Melting was carried out in vacuum and purified argon, respectively. Although uncontaminated by the atmosphere, reaction between the molten alloys and their containers at 1150 to 1200°C undoubtedly takes place. In this investigation, the need for a container, refractory or otherwise, was eliminated by the use of a "floating zone" technique. A molten zone was established between two vertical cylindrical rods of the cast iron eutectic material and was supported by the surface tension of the liquid. Liquid was in contact only with vacuum and solid iron-carbon alloy of the same composition.

Close control was also afforded by the floating zone technique. Unlike the previous investigations(26, 37) in which nucleation occurred on the mould walls, the floating zone technique eliminated heterogeneous nucleation sites ahead of the solid-liquid interface and growth was confined to that interface.

Because a vacuum of better than 10^{-4} mm of Hg was attainable and the evaporation loss of the eutectic liquid was low due to the low vapour pressure at the eutectic temperature, heating by electron bombardment was chosen. As pointed out by Schadler(66), who recently reviewed the use of the floating zone technique for growing single crystals of high melting point materials, electron bombardment affords better control over zone length than either induction or radiation heating.

5.2 Apparatus

A photograph of the electron-beam floating zone melting apparatus is shown in Figure 14. Construction was carried out at McMaster University by Mr. H. Walker under the direction of Dr. G. R. Purdy. The electrode assembly was designed and built by the author.

5.2.1 Vacuum Chamber

The chamber was constructed from a cylindrically shaped seamless mild steel pipe 11 inches inside diameter with a ½ inch wall and 6½ inches long. The inside surface was machined round and honed to a bright scratch-free surface. "0"-ring grooves were machined in the front and back of this cylindrical pipe. The top and bottom were milled flat and circular holes 2½ inches in diameter were milled in the top and bottom with their centres 2½ inches from the rear edge. These holes, covered by square brass plates ½ inch thick containing "0"-ring grooves, facilitated the introduction of the electrode assembly which will be discussed later. The back was machined from a 7/16 inch mild steel plate and contained a 2 inch vacuum port and two holes for electrical leads. Vacuum sealed high voltage electrodes supplied by Edward's High Vacuum were used. The vacuum pumping system, which was connected to the chamber by 2 inch diameter wrought copper pipe, consisted of a 2 inch water-cooled oil diffusion pump backed by a mechanical pump with a capacity of the order of 50 litres per minute. A typical vacuum maintained throughout the solidification runs was 5×10^{-4} mm Hg as measured by an ionization gauge.

The front of the chamber was covered by a ½ inch thick aluminum plate which was hinged to facilitate entry when air was admitted. An 8 inch viewing port was included in the front panel to facilitate close observation of the zone and measurement of the rate of solidification. This port was covered by 3/4 inch thick "armour" glass, capable of withstanding open-flame temperatures as high as 500°F. An aluminum foil radiation shield could be manipulated from outside the vacuum system.

A drawing of the electrode assembly is shown in Figure 15. In this apparatus, the sample remained stationary and the electrode moved relative to it on a twin I - beam track. The idler wheels were equipped with ball bearings and the assembly traversed both up and down very smoothly and with close tolerances. Motion was transmitted by the windlass assembly shown. The drum on which the dead-soft copper wire was wound was powered by an electric motor and variable-speed transmission. The shaft entered the vacuum system through a Wilson seal.

Traverse speeds from 2 to 10,000 mm per hour were attainable although rates higher than 800 mm per hour were used only during the process of setting up and sample adjustment. The rate of 800 mm per hour was the maximum at which a stable zone could be maintained. A cathetometer was used to measure the traverse speed for each run.

Teflon was chosen as the structural material for supporting the electrode because of its excellent dielectric, vacuum and thermal properties. The choice of materials is very restricted because the structure must withstand temperatures of the order of 200°C and potentials of 2000 volts while under vacuum. Evaporation "umbrellas" were placed on both electrical leads through the teflon so that evaporated metal films would not short-out the filament. A radiation shield was placed between the filament and the teflon. After continued use, evaporated deposits built up to the point that discharge occurred but the teflon was not damaged. Initially, fired pyrophyllite was employed instead of teflon but electrical discharge quickly impaired its dielectric properties and rendered it unserviceable.

The cathode consisted of a 0.010 inch diameter W wire of a design similar to Calverley et al(67) clamped at both ends to vertical 1/8 inch drill rod electrical leads. Molybdenum focusing shields were clamped above and below the filament and were independently adjustable on the drill rod binding posts. This increased flexibility enabled adjustments to be made after initial stress relief and high temperature creep of the filament without disturbing the embrittled tungsten.

The samples were held in aluminum spring-loaded V-blocks mounted on Alnico horse-shoe magnets. Bolt holes were spark machined in the magnets. The magnetic sample holders provided great ease of handling and alignment, especially with bent samples, and facilitated the removal of the melted rods. The magnets were insulated from the chamber by asbestos tape and the sample current was monitored on a milliammeter.

5.2.2 Electronics

A block diagram of the electrical circuit required for electron-bombardment melting patterned after Calverley et al(67) is shown in Fig. 16. The essential features are the emitter and focusing arrangement already discussed, the high voltage power source, the filament power source and a means for controlling the power. The latter is achieved via the bombardment current which is controlled in turn by the thermionic emission from the cathode with voltage fixed, or by voltage control, wherein the bombardment current is held constant and the voltage varied. The first approach is simpler and has therefore been almost exclusively used.

The emission current is controlled by comparing it to a standard potential which is in turn controlled by the operator. The amplified difference in potential controls the filament power through a control circuit. A thyratron circuit after Calverly et al(67) is shown in Fig. 17. In addition, a saturable reactor(66) and a motor driven Variac control system(68) have been used in the past. The thyratron control of Calverly et al(67) was chosen because of its simplicity and its rapid response to changing conditions such as gas evolution from the sample.

Although the circuit is self stabilizing, power regulation was found to be necessary in order to achieve long time stability of the molten zone. A Sola constant voltage power transformer was used with excellent results to supply power to the 2 KV high voltage transformer, the power transformer, and the control circuit.

5.3 Summary

The block diagram of Fig. 16 and the control circuit of Fig. 17, both after Calverly et al(67), were readily converted to North American power supplies. The high voltage supply was a variac controlled full-wave rectified circuit using 866 A rectifying tubes while the 0-300 V D.C. control voltage was supplied by a solid state rectifier circuit. The thyratron control circuit was identical to Fig. 17 with the exception of 5557 thyratron tubes.

With the incorporation of a Sola line stabilizer, stability was excellent and control was accurate and rapid. In this apparatus, close experimental control of the solidification variables was realized while at the same time the purity of the specimen was maintained.

CHAPTER 6

EXPERIMENTAL TECHNIQUES

6.1 Materials and Sample Preparation

The base materials, iron and carbon, were chosen to produce melts of high purity with reasonable regard to economy. Initial experiments were carried out with cast iron produced from Armco iron and semiconductor grade graphite (National AUC grade). Table 1 gives the composition of the resultant alloy. In addition, a melt of Westinghouse "Puron" and graphite was prepared. Table 2 gives the composition of this alloy.

In the production of Ni-C alloys, nickel of 99.9% purity was used with the AUC graphite to produce an alloy of eutectic composition. Ternary Fe-C-Si alloys were prepared by the addition of 99.9% purity Si, with the main impurity being iron to an Armco melt. The composition of the Fe-C-Si alloy is given in Table 3.

All of the alloys were melted in graphite crucibles heated by induction heating. Fig. 18 is a schematic illustration of the apparatus and experimental arrangement used in producing the alloys. The crucible was 5 1/8 inches in diameter and was made of high purity "National AUC" grade graphite. A two inch hole was machined in the graphite block to receive the iron melting stock. Heating was accomplished by the 3000 cycle induction coil shown, with the graphite serving the double purpose of susceptor and carbon source. Melting was carried out under argon in the graphite hood shown. The vycor top plate facilitated visual scrutiny of the melt preparation.

After the iron was molten, the melt was maintained at a temperature slightly above the eutectic temperature until carbon saturation occurred. The temperature was then decreased slowly so that the kish (hyper-eutectic graphite) could precipitate and float to the top. The eutectic temperature was detected by observing the initial solidification of the eutectic alloy. Initial freezing occurred at the top of the melt where radiative heat losses were greatest. The alloy was then superheated about 50 to 100°C, the kish was skimmed with a graphite "spoon", and samples were taken. Reference to Fig. 7 indicates that the graphite-liquid equilibrium solubility line has a very steep slope so that the slight superheat results in a composition which deviates from the eutectic value by a negligible amount.

Specimens for melting by the floating zone technique must be long straight cylindrical rods with smooth surfaces and a high degree of long-range chemical homogeneity. A diameter of 1/8" was chosen as the most suitable for the apparatus discussed above. Eutectic Fe-C, Ni-C, and Fe-C-Si rods were prepared by sucking molten eutectic liquid into evacuated pyrex tubes followed by quenching in water. In the case of the binary Fe-C alloy, the product was a white cast iron. The Ni-C alloy solidified with a graphitic morphology because there appears to be no stable carbide at 1 atmosphere pressure(69) and the Fe-C-Si alloy had a mottled structure. All specimens had the required physical, chemical and surface properties and were subsequently used in the "as-quenched" condition.

6.2 Electron Beam Melting

A solidification run was started by establishing a molten zone in the 1/16 inch gap between the two cast iron rods held vertically in their V-block holders. The gap between the two rods tended to reduce buckling of the sample due to thermal expansion and maintained the volume of metal in the zone at a manageable size. In the Fe-C alloys which were completely carbidic, solidification in the metastable (white iron) mode was achieved by accelerating the zone to the desired rate immediately after establishment of the zone. To investigate grey iron solidification, the molten zone was held fixed for ½ hour in order to produce a graphite substrate through the solid state decomposition of cementite, upon which graphitic eutectic structures would nucleate and persist. The mode of solidification, either white or grey, was clearly evident from the surface quality of the sample, being highly reflective for white but rather dull for grey iron solidification.

In all experiments, the zone was passed in the upward direction in an attempt to minimize convective mixing at the solidifying (lower) interface. This mode presented no problems of zone instability, presumably because of the high surface tension of the alloys. Cast iron rods produced in the manner mentioned above were relatively free of blow holes and dissolved gas so that an initial degassing pass was not necessary.

6.3 Metallographic Preparation

The metallographic preparation of grey cast iron can present difficulties due to the erosion of the soft graphite flakes during abrasion and lapping. The most important feature of the polishing technique is the minimization of polishing time.

All the iron base specimens were mounted in bakelite and were abraded in successive steps through 220, 320, 400, and 600 grit silicon carbide paper with water lubrication. Initial lapping was carried out with 8 micron diamond paste on a short napped cloth with kerosene as a lubricant. The second stage consisted of gentle hand lapping under similar conditions with 1 micron diamond for a period of 30 seconds to 1 minute. The final polish was obtained on the "Syntron" using 0.3 micron alumina slurry for periods from 15 to 30 minutes. In the nickel base alloys, the 1 micron diamond polish was not used but the alumina slurry treatment was extended to one hour. The graphitic samples were not etched.

The white iron samples were polished using standard metallographic techniques. After abrasion and an 8 micron diamond polish, the samples were placed in a 0.3 micron alumina slurry in the "Syntron" for periods up to 3 hours. Five percent nital was used as etching reagent.

In the series of experiments to determine interlamellar spacing as a function of growth rate, the above metallographic techniques were used. The samples were polished on a plane perpendicular to the growth direction so that the lamellae intersected the polished surface at right angles. The number of lamellae cutting the surface per unit length was determined at 10 points on each section polished and these results were averaged and accepted as one result. Distances were measured with a double cross-hair eye-piece calibrated with a stage micrometer. The sample was abraded and polished 10 times and spacing measurements were taken each time. The standard 1σ deviation was calculated from the 10 averaged results.

6.4 Electron Microscopy

Transmission electron microscopy of extracted graphite nodules was carried out to determine the growth front orientations. Extraction of the spheroids was achieved by dissolving the metallic matrix in acid and decanting the excess liquid. The Ni-C alloys were dissolved in a 33 percent solution of nitric acid by volume in ethanol while the Fe-C-Si alloys were dissolved in an aqueous hydrochloric-nitric acid solution. After complete dissolution, the acids were decanted and the spheroids were rinsed with distilled water. Spheroids were sprinkled on a formvar substrate and examined in a Siemens electron microscope at 100 KV.

Because of the spheroidal shape and large size of the graphite nodules, electron transmission occurred only at the periphery of the equatorial plane of each nodule where the spheroid was thinnest.

Selected area electron diffraction was carried out and diffraction patterns were related to growth facets observed in electron micrographs of the same areas. The crystallographic orientation of graphite in the nodule was determined in this way.

6.5 Temperature Measurement

An attempt was made to measure the undercooling at the solid-liquid interface as a function of solidification rate. Because of the hot tungsten filament in the electron bombardment apparatus, optical pyrometric techniques could not be used and because of the electron bombardment, a thermocouple could not be mounted externally on the samples.

To overcome these difficulties, the 1/8 inch white iron rods were graphitized and a 0.055 inch hole drilled down the centre. Graphitization of the white iron took place by the solid state decomposition of Fe_3C at 1050^oC in an inert argon atmosphere provided by sealed-off quartz capsules. A platinum-platinum 10% rhodium thermocouple and quartz protection sheath were inserted in the drilled hole so that the complete molten zone passed over the thermocouple bead and the temperature profile of the whole zone was given. The quartz protection sheath was hand drawn capillary tubing about 0.050 inches outside diameter and 0.040 inches inside diameter. The 0.005 inch thermocouple wires were separated by a single bore mullite ceramic insulator 0.031 inches outside diameter and 0.020 inches inside diameter. The thermocouple and protection sheath assembly is shown schematically in Fig. 19.

The thermocouple emf was backed off with a variable direct current supply from a storage battery and displayed on a recorder with a scale reading from 0 to 1 millivolts. The interface temperature was identified by a change in slope on the recorder chart and was measured for a series of rates. In this experiment, the absolute temperature was not measured because of the difficulty of introducing a standard thermocouple into the electron-beam melting system. In addition, the variable bucking emf necessary to display the thermocouple output on a recorder scale which covered the range 0 to 1 millivolt presented further difficulties in measuring the true temperature. However, because all the profiles showed identical characteristics at the melting interface, the temperature change, ΔT, was determined by comparing the temperature of the freezing interface to the temperature of the melting interface which remained unaffected by freezing rate and thus indicated the true eutectic temperature. In all cases, care was taken to ensure that the same material, either graphitic or carbidic, was melted and solidified so that the ΔT values represent the undercooling below the eutectic temperature of the appropriate mode. A copper cooling block was silver-soldered to the lower half of the rod in order to steepen the thermal gradient and cause a more abrupt change in slope at the solid-liquid interface.

Reaction between the quartz protection sheath and the melt was not a serious problem because of the short exposure time and the slow kinetics of the reaction

$$SiO_2 + 2C = Si + 2CO$$

at 1155°C (87). Indeed, no evidence of CO evolution was observed in this system.

6.6 The Temperature Profile

As outlined above, the temperature profile of the whole zone was obtained in attempting to measure the undercooling at the solidifying interface. Fig. 36 is a reproduction of the strip chart indicating the emf from the thermocouple as a function of distance in the sample for one of the experiments carried out.

Several features of Fig. 36 are of interest. Firstly, the upper end of the molten zone is approximately isothermal and secondly, the temperature gradients in the solid are steeper than in the liquid. Since the latent heat is small and since the thermal conductivity in the liquid is smaller than in the solid, we expect the opposite behaviour if thermal conductivity is controlling. At the low temperatures associated with molten cast iron, radiation heat loss is not appreciable so we are unable to attribute the unusual temperature distribution to this cause. These observations can be rationalized only on the basis of strong convective mixing in the molten zone which acts as a heat flow mechanism in parallel with the conductive flow. Indeed, strong convective currents have been observed in the zone by watching the motion of alumina particles adhering to the surface of the molten liquid. The result is a flattening of the temperature profile in the liquid to the point that the gradients are less there than in the solid where conduction is the primary heat transport mechanism. Although the conductivity coefficient in the solid is higher than in the liquid,leading to lower gradients in the solid, the parallel heat flow characteristics of the liquid are sufficient to reverse the trend and flatten the gradients in the liquid. In Fig. 37, a schematic drawing of the cross-section of the system is used to indicate the manner in which convective mixing can occur. On the right of the drawing, approximate isotherms are indicated and on the left, the direction of mass flow is indicated. Convection is initiated in the upper half of the zone as a circular motion driven by the lower density of the liquid at the hot centre. Viscous coupling in the liquid leads to convection of lower intensity in the bottom. The result is a system consisting of two vortices of molten liquid as shown on the left of Fig. 37.

The resulting smoothed temperature profile (cf. Fig. 36) showing rather small inflections made the location of the solid-liquid interfaces in relation to the temperature very difficult. In estimating the undercooling, the interface has been located as the temperature points where the curve begins to deviate strongly from the linear behaviour expected in the solid. This point was not too clearly defined at the melting interface but a distinct inflection was usually observed at the solidifying interface.

Some variation in the liquid temperature gradient was observed between runs due to variations in the physical arrangement of the system. There is no theoretical reason to believe that this should have any effect on the spacing. Indeed, Yue(6) has shown that the temperature gradient in the liquid in the range from 9 to 50°C per centimeter has no effect on the interlamellar spacing in the Aℓ-Mg eutectic system. We suppose here, even though our gradients are much higher, the same independence of spacing and liquid gradients.

CHAPTER 7

RESULTS AND DISCUSSION

7.1 Morphology

7.1.1 Morphology of Fe-C Eutectic Alloys

The solidification morphologies in both the eutectic Fe-C and $Fe-Fe_3C$ systems have been studied as a function of growth rate using alloys with the purities listed in Tables 1 and 2. Studies of the Fe-C system have been confined to the range 2 mm/h to 110 mm/h because the first figure represents the slowest growth rate attainable with the apparatus discussed above and the second figure is the rate at which the stable Fe-C system transforms to the metastable $Fe-Fe_3C$ system. This transformation will be discussed in Section 7.5.

Fig. 20 is a photomicrograph of the graphite-austenite eutectic solidified directionally at 2.0 mm/h. The high degree of directionality of the graphite flakes parallel to the growth direction is immediately apparent. Although some branching and flake distortion has occured (probably due to instability in the apparatus), this structure appears to be a continuous lamellar array of graphite flakes and what was initially austenite. Upon increasing the solidification rate, the regular lamellar structure of Fig. 20 becomes more highly branched and looses directionality. Fig. 21 shows the result of these latter tests corresponding to 18.1 mm/h for the alloy of Table 1. This lacy graphite morphology is observed up to solidification rates of 110 mm/h with the structure becoming increasingly fine. The appearance of strips of graphite enrichment in Fig. 21 arises from the fact that the alloy could not sustain a stable planar front under steady-state growth conditions. The interface has accordingly developed a cellular character, accompanied by the segregation of carbon to the cell boundaries. The cell boundaries are outlined by the graphite enrichment appearing in Fig. 22, which was prepared from a section at right angles to the growth direction. These lacy graphite structures are similar to those reported by Lakeland(36) who attributes the instability to trace amounts of sulphur(88). This indeed seems to be the case because Fig. 23 represents a sample of lower sulphur content (see Table 2) which shows a less pronounced cellular structure when grown at 60 mm/h. A cellular structure in this purer alloy was not observed until growth rates of the order of 50 mm/h were attained. Morphology results in the Fe-C system were reported concurrently by Lakeland(37) and ourselves(27).

In addition to the Fe-C system, observations in the metastable Fe-Fe_3C system have also been carried out with results similar to those of Wilkinson and Hellawell(26). Over a wide range of growth rates from 50 to 600 mm/h, a regular lamellar structure has been observed. Fig. 24 represents a typical result in the Fe-Fe_3C system corresponding to a growth rate of 60 mm/h. It is important to note that the structures of Figs. 23 and 24 were produced under identical steady growth conditions using the same alloy and the same apparatus. Their history differs only in their initial conditions. The carbidic structure of Fig. 24

was grown from the as-cast white iron substrate while the graphitic structure of Fig. 23 was grown from a graphite nucleus provided by the decomposition of Fe_3C in the high temperature region adjacent to the molten zone. At rates less than 50 mm/h, Wilkinson and Hellawell(26) observed a mottled structure. In this investigation of the $Fe-Fe_3C$ system an instability at low growth rates was observed which will be discussed in Section 7.5.

7.1.2 Morphology of Ni-C Eutectic Alloys

A high purity Ni-C eutectic alloy has been solidified directionally at growth rates ranging from 20 to 450 mm/h. Solidification of this alloy has many characteristics in common with the Fe-C alloys but is less complicated because there is no metastable phase at atmospheric pressure and the austenite does not undergo a low temperature phase change analogous to the pearlite reaction in the Fe-C system.

Fig. 25 shows a typical directional lamellar graphite flake morphology obtained by solidification at 24 mm/h. The degree of perfection of this sample is very high and compares favourably with the lamellar Fe-C morphology of Fig. 20 which was grown at a rate which was slower by a factor of 10. An increase in solidification rates causes a transition from a lamellar to a lacy graphite morphology analogous to the Fe-C system. Fig. 26 is a typical lacy graphite morphology in the Ni-C system. In this structure, the graphite is a continuous phase but the degree of branching is very high and the structure shows almost no directionality when solidified at a growth rate of 180 mm/h.

A further increase in growth rate beyond 330 mm/h is accompanied by a sudden change to a discontinuous nodular graphite morphology. Fig. 27 shows a typical nodular morphology consisting of well formed graphite spherulites obtained at a solidification rate of 440 mm/h. It is interesting to note that modification in the Ni-C eutectic system can be brought about simply by an increase in solidification rate and without the addition of a nodularizing agent. Similar experiments suggest themselves in the Fe-C eutectic system.

7.1.3 Morphology of Fe-C-Si Eutectic Alloy

As mentioned above in Section 7.1.1, the graphite-austenite eutectic mode transforms to the metastable iron carbide-austenite eutectic mode at solidification rates greater than 110 mm/h. Therefore, in order to study graphite morphologies at high solidification rates, a ternary Fe-C-Si eutectic alloy was used with the composition given in Table 3. The Fe-C and Fe-C-Si alloys have identical lamellar and lacy graphite morphologies at slow solidification rates. Figures 28 and 29 show the morphologies at solidification rates of 670 and 860 mm/h respectively. Although the structures are mainly lacy graphite, some nodules appear at both rates with a higher proportion occurring at the higher rate. A comparison of Figures 28 and 29 indicates that the lacy graphite of Fig. 29 is less continuous and has some similarities to the modified structure. Although 860 mm/h was the maximum solidification rate at which the melting zone could be kept intact, these results indicate that an increase in solidification rate alone can lead to a spheroidal modification.

Since the surface free-energies are not expected to change with growth rate, modification probably results from a change in growth kinetics of the graphite in the system as discussed in Section 4.5.2. As the solidification rate is increased, the partition of sulphur to the graphite phase becomes increasingly difficult. When the sulphur content in the graphite drops below a critical value, the thickening of graphite plates is no longer inhibited sufficiently to produce supersaturation and re-nucleation of graphite with a new orientation on the original graphite nucleus. This condition of inhibited basal plane growth under which lacy (or fine flake) graphite is produced is progressively removed with increasing solidification rate and the spheroidal morphology results at high growth rates. This is certainly the case in the Ni-C eutectic system where complete modification was observed with only a change in growth rate. In the Fe-C-Si system where only partial modification resulted from an increase in growth rate, the same agrument applies although the possible role of surface free-energy changes cannot be discounted without further evidence. The great effect of sulphur on the surface tension of cast iron has already been pointed out(60).

Desulphurizing experiments were carrried out in a static system in which a molten sphere of cast iron was suspended by surface tension from the end of the top rod in the electron bombardment apparatus. By rapidly turning off the electron-beam, these molten masses solidified at an estimated rate of 500 mm/h from both the top and bottom. Untreated as-quenched samples had a structure similar to Fig. 28.

Desulphurization was carried out using Na_2O (89) and solid CaO (90) which are strongly desulphurizing slags under the conditions imposed and capable of reducing the sulphur content to approximately 0.003%.(90) Neither treatment affected the morphology greatly, although the density of nodules was increased slightly so that a structure similar to Fig. 29 resulted. On the other hand, when sulphur was added in the form of FeS, a completely lacy structure resulted at a solidification rate of 500 mm per hour with no nodules appearing in the microstructure. On the other hand, the addition of cerium in the form of pure metal resulted in the completely nodular structure of Fig. 30.

The conditions under which modification in the ternary Fe-C-Si takesplace are now quite clear. The nodularizing agent performs the function of reducing the residual sulphur concentration in the solution and thereby changing the growth kinetics of the graphite. A reduction of residual sulphur to 0.003% by desulphurization is sufficient to change the surface tension appreciably(60) but does not affect the morphology. The effect of sulphur in inhibiting spheroidization has been demonstrated and the proposed mechanism of inhibition accounts for the experimental findings. Barton's(82) observation that a low sulphur content is a prerequisite for modification has been confirmed. The role which sulphur plays can not be attributed to its marked effect on the surface tension of cast iron(60).

We must concur therefore with Minkoff(59) that a change in growth kinetics is the important factor in nodular graphite production although the proposed mechanisms differ. The surface free-energy change resulting from the addition of the modifying agent is of secondary importance and only a consequence of the reduced sulphur concentration brought about by reaction of the sulphur with the modifying agent to produce stable sulphides. Although the Ni-C eutectic system can be modified by growth rate alone, the nodularizing agent is an essential feature in the Fe-C system where unreasonably high growth rates have produced only a partially modified structure.

7.1.4 Summary of Growth Morphologies

In the iron carbide-austenite eutectic, white cast iron, regular continuous lamellar structures were observed at all growth rates greater than 50 mm/h. The decrease of interlamellar spacing with increasing solidification rate will be discussed in Section 7.3.

In the graphitic Fe-C, Ni-C and Fe-C-Si alloys, an increase in growth rate was accompanied by a morphology change from lamellar flake graphite to a fine, highly-branched, lacy graphite structure. In the Ni-C and Fe-C-Si alloys, a further increase in growth rate resulted in a completely nodular and a partially modified graphite morphology respectively.

The addition of Mg or Ce to eutectic cast iron leads to modification of the graphite morphology by reducing the residual sulphur concentration to the extent that thickening of basal planes by a screw dislocation mechanism is not inhibited and these planes dominate the crystallography and produce a spheroidal morphology. A low sulphur concentration is a prerequisite for nodule formation(82) but desulphurizing experiments have shown that the resulting change in surface properties with decreasing sulphur concentration cannot be considered important in the formation of nodules in cast iron.

7.2 Electron Microscopy of Graphite Nodules

The observations in Fe-C-Si and Ni-C that a nodular morphology results from a high growth rate made a determination of the crystallographic orientation of the graphite in the nodules advisable. Under the condition of high growth rate, a nodular morphology bounded by high index fast-growing planes seems intuitively more reasonable than a similar structure bounded by low index slow-growing planes although the latter structure was determined by X-ray diffraction(58) and polarized light observations(11).

Because the nodules are roughly spherical and exhibit radial symmetry, a determination of the crystallography at the periphery of the equatorial plane is sufficient to determine the whole structure since the nodules are randomly orientated on the electron microscope grid. The observation of an [00.1] zone diffraction pattern would indicate a nodule bounded by high index planes while the observation of an [uv.0] zone diffraction pattern would necessitate relating the electron diffraction pattern to an electron micrograph of the same spot.

Fig. 31 is an electron micrograph of a graphite nodule which presents a projected profile of the shape at a magnification of 20,000 times. Nodules extracted from Fe-C-Si and Ni-C alloys have been studied and the characteristics shown in Fig. 31 are common to all nodules. These features include the approximate projected hexagonal shape with 120 degree corners and pyramidal growth facets on the otherwise flat sides. Selected area diffraction was carried out on these growth facets since the sample was thin enough at these points for electron transmission.

Fig. 32 is a diffraction pattern taken from the facet of Fig. 31. Diffraction is uneven because of the sample thickness and many of the extra spots result from diffraction by other crystals. Multiple diffraction is to be expected in polycrystalline graphite nodules. Nodules from both the Fe-C-Si and Ni-C alloys produced identical diffraction results. Because the diffraction pattern of Fig. 32 does not represent an [00.1] zone, the spots were indexed as shown in Fig. 32 in an attempt to relate the diffraction pattern to the electron micrograph of Fig. 31. Shapiro(91) has facilitated relating the diffraction pattern to the electron micrograph by determining the angle of rotation between these two images in the Siemens electron microscope at McMaster. At a magnification of 20,000 times, the electron micrograph is rotated clockwise with respect to the diffraction pattern by an angle of 26 degrees. When Fig. 32 is rotated clockwise by an angle of 26 degrees, the [0004] direction of the diffraction pattern is perpendicular to the planes bounding the growth facet. The growth facet is bounded therefore by (0001) planes which supports the original observation that graphite spheroids are bounded by basal planes.

As stated above, similar growth shapes and electron diffraction patterns were obtained with nodules extracted from both the Fe-C-Si and Ni-C alloys. It therefore seems probable that the growth mechanism of graphite nodules is the same in both systems with growth occurring in such a manner that the resulting nodule is bounded by basal planes.

7.3 Interlamellar Spacing

The results obtained for the interlamellar spacing as a function of growth rate are summarized in Fig. 33 for both the stable Fe-C and metastable Fe-Fe_3C eutectic systems. The numerical results are tabulated in Table 4. The experimental points with error bars were obtained in this investigation while the other results were taken from Lakeland(37) and Wilkinson and Hellawell(26) for the Fe-C and Fe-Fe_3C systems, respectively. The agreement in both cases is excellent.

In the Fe-C system, the results of Lakeland(37) have been fitted statistically to the relationship

$$\lambda = AR^{-n}$$

yielding a value of the exponent $n = 0.495$. The limited number of experimental points determined in this investigation give a value of $n = 0.59$, as shown, but reference to Fig. 33 indicates that all the data are consistent. Because of the larger number of determinations by Lakeland(37), a value of $n = 0.5$ is probably representative of this system. It is interesting to note that Lakeland's results were obtained with Fe-C eutectic alloys solidified in a horizontal refractory boat while in this investigation, solidification occurred in a vertical system with no crucible. The rate of 110 mm/h at which the Fe-C eutectic transforms to the Fe-Fe_3C eutectic system is indicated on the diagram.

The results of Wilkinson and Hellawell(26) in the Fe-Fe_3C system are best described by an exponent value of $n = 0.35$ while the results of this investigation indicate $n = 0.38$ over the range of growth rate from 60 to 600 mm/h as shown in Fig. 33. At growth rates less than 60 mm/h, uniform interlamellar spacings were not observed throughout the whole sample. At these slower rates, a gradation from fine to coarse spacing was observed from the outside to the centre of the samples and in some cases the centre was graphitic. These results are completely consistent with Wilkinson and Hellawell(26) who observed graphite in samples grown at rates less the 40 mm/h. In addition, their results plotted in Fig. 33 show a wide scatter at slow growth rates indicating an instability associated with these growth conditions.

Cooksey et al(92) have reviewed the published date on directionally solidified eutectic systems and have found only four systems, Aℓ-Zn, Ag-Cu, Fe-Fe_3C, and Mg-Aℓ, in which the exponent, n, approximated to 0.35 in the above relationship. In all other systems, a value of $n = 1/2$ has been approximated in agreement with the theoretical development of Tiller(1). The present investigation is unique in that two eutectic systems, the Fe-C and the Fe-Fe_3C systems, were studied using materials of the same composition and purity at the same temperature under identical experimental conditions. In these systems, the two rate laws, $R^{-1/2}$ and $R^{-1/3}$, have been observed (see Fig. 33). One must therefore conclude that the $R^{-1/3}$ relationships are significant and not just the result of some experimental variable such as convective mixing of the melt(73). Although convective mixing has been observed in the electron-beam system, it was noted in Section 6.6 that this transport mechanism is minimized at the freezing interface by solidifying the samples upwards in a vertical system. Under these conditions, the width of the stagnant boundary layer at the lower interface is expected to be sufficient to eliminate convective effects. Indeed, the observation of an $R^{-1/2}$ relationship in the Fe-C system confirms this expectation.

This result is of great interest in the light of the theoretical approaches outlined in Chapter 2. At that time, the limitations of the theories leading to the $R^{-1/2}$ law were pointed out. It now becomes clear that the theory of lamellar eutectic solidification must be detailed enough to account for the two rate laws, $R^{-1/2}$ and $R^{-1/3}$, which have occured in the two iron-carbon systems under identical growth conditions.

7.4 Undercooling at the Solid-Liquid Interface

In addition to determining the interlamellar spacing as a function of solidification rate, the undercooling at the solid-liquid interface was measured for a number of rates. The results are shown in Fig. 34 and Fig. 35 of the Fe-C and Fe-Fe_3C systems, respectively. A reproduction of a typical strip chart from which the undercooling results were obtained is given in Fig. 36, indicating emf (which is directly proportional to temperature) as a function of distance.

Several features are immediately apparent from Fig. 36. The first and probably most interesting feature is the very small amount of superheat to which the molten zone is subjected. The temperature of over half the molten zone is approximately 2°C above the eutectic melting temperature, which is indicated on the chart by the change in slope. This uniformity of the temperature profile undoubtedly results from convective mixing in the upper half of the zone where an inverse temperature gradient exists as discussed in Section 6.6. In the lower half of the zone, the temperature decreases gradually to the solid-liquid interface temperature which is indicated by a change in the slope of the graph. The temperature gradient was maintained as steep as possible by the use of a copper cooling block in order to accentuate the change in slope at the interface. However, it is obvious from Fig. 36 that a considerable error could result in choosing the interface position and this error would in turn be present in the undercooling measurements. In Fig. 34 and Fig. 35, the estimated error in recording the undercooling was indicated on the graphs. These errors are subjective estimates based on the accuracy to which the inflection in the chart record could be pin-pointed. The accuracy of the undercooling measurements decreases with increasing solidification rate up to 200 mm/h, which is the upper limit for this technique. At rates greater than 200 mm/h, mechanical instability of the zone was frequent and the interface position could not be established accurately. Solidification rates were measured independently with a cathetometer.

The shape of the temperature profile shown in Fig. 36 differs markedly from the results of Hunt and Chilton(74) who measured the undercooling at the solid-liquid interface in the Pb-Sn system. However, the definite inflection which these authors observe in the temperature profile can be readily recognized although it is not entirely consistent with steady-state heat flow considerations. On the other hand, Fig. 36 represents a true steady-state heat flow profile but presents the serious difficulty of determining the interface position accurately.

Fig. 34 and Fig. 35 are not inconsistent with a parabolic variation of undercooling with rate of the form

$$\Delta T \alpha R^{1/2}$$

predicted by Tiller(1) and observed by Hunt and Chilton(74) in the Pb-Sn eutectic system. Thus, the results obtained for the stable Fe-C system in this experiment can be reconciled with existing postulates and the resulting equations. However, inconsistency is apparent if both the Fe-C and $Fe-Fe_3C$ eutectic systems (which were found to obey the relationships $\lambda^2 R$ = const and $\lambda^3 R$ = const, respectively) do indeed obey an undercooling versus rate relationship of the form $\Delta T \alpha R^{1/2}$. As indicated above, a more penetrating theoretical description is needed to explain the experimental observations.

7.5 Transformation of the Solidification Mode

A transformation from the stable Fe-C to the metastable

$Fe-Fe_3C$ eutectic mode with increasing solidification rate was anticipated in Section 3.3. The results of this investigation have been summarized in Fig. 33 and Fig. 34. The transformation has been observed to occur completely reproducibly at a steady solidification rate of approximately 110 mm/h.

The product of this transformation from fine lacy graphite is a regular lamellar array of carbide and austenite phases with an interlamellar spacing characteristic of the transformation rate. After carbide nucleation, the metastable phase grows rapidly and dominates the morphology.

Although the transformation from the stable to the metastable mode occurs consistently in the pure eutectic iron-carbon alloy, the transformation is not reversible. When the $Fe-Fe_3C$ eutectic system is solidified at rates less than 110 mm/h, the morphology and solidification characteristics are similar to those at high solidification rates. This is true to solidification rates of the order of 40 to 50 mm/h. At slower rates, instability of the regular lamellar carbide phase occurred. In this investigation, interlamellar spacings could not be measured at rates slower than 50 mm/h because of the onset of non-uniformity in the specimens. Reference to Fig. 33, in which the interlamellar spacing versus rate results of Wilkinson and Hellawell(26) are shown as full circles, indicates a large scatter in the experimental points at slow rates, also indicative of instability. These authors also observed mottled structures at solidification rates below 40 mm/h. In this investigation, graphite was also observed in the centre of carbidic samples at slow solidification rates.

The explanation for this instability can be found in the undercooling results (Fig. 35) and the phase diagram (Figs. 6 and 7). As indicated in Fig. 35, the undercooling at the interface in the Fe-Fe$_3$C system at a solidification rate of 40 mm/h is approximately 5°C. Reference to the phase diagram (Fig. 8a) and the free energy-composition diagrams (Fig. 8b-f) indicates that this undercooling is approximately equal to the temperature difference between the Fe-Fe$_3$C eutectic temperature and the intersection of the liquid-graphite and liquid-cementite solubility lines, temperatures T_2 and T_4, respectively. As discussed earlier in Section 3.3, both the Fe-C and Fe-Fe$_3$C modes can occur in this temperature range from T_2(1149°C) to T_4(1144°C) but the Fe-C mode is more probable because of its higher supersaturation. Graphite has been observed to nucleate at the slow rates(26, this investigation) which exhibit undercoolings characteristic of this temperature range,but the growth of graphite seems to be the controlling factor in this metastable to stable transition with decreasing solidification rate. Because after it is nucleated graphite does not grow rapidly enough to dominate the morphology, a mottled structure results with the graphite discontinuous in a carbide matrix. Hillert(18) has already drawn attention to the ease of nucleation but the slow growth characteristics of graphite in cast iron.

The conditions under which both transformations occur can be completely understood on the basis of this investigation. Although the stable to metastable transformation is irreversible with respect to rate, undercooling results indicate that both the stable to metastable and metastable to stable transformations occur at the same temperature; the intersection of the liquid-graphite and liquid-cementite solubility lines. The first transformation is kinetically favourable and goes to completion while the second is kinetically unfavourable and only the nucleation and initial growth products are observed in the resulting structure. The transformation is not reversible at the solidification rate of 110 mm/h because eutectic temperatures for the Fe-C and Fe-Fe_3C modes differ by 5°C (Fig. 7) or 6°C (Fig. 6) while the undercooling as a function of rate is almost identical in both modes.

In summary, the temperature at the interface in the Fe-C eutectic system decreases from 1155°C to 1144°C as the solidification rate is increased from 0 mm/h to 110 mm/h. At this solidification rate, carbide is nucleated and grows to dominate the morphology,but at a temperature of approximately 9°C below the Fe-Fe_3C eutectic temperature taken to be 1149°C (see Fig. 35). The stable to metastable transformation at constant rate is accompanied by a 5°C decrease in temperature of the whole system. When the solidification rate of white iron is decreased to 40 mm/h, the temperature at the interface is 1144°C which is characteristic of a 5°C undercooling. At approximately this temperature graphite has been observed to nucleate but the metastable to stable transformation does not dominate and the Fe_3C mode is retained to even slower solidification rates.

7.6 The Iron-Carbon Phase Diagram

The iron-carbon phase diagram has been determined except for the liquid-cementite solubility line(16). As outlined in Chapter 3, Hillert(18, 21) has predicted that this solubility line is much more horizontal than previously thought due to the low melting point of Fe_3C at 1207°C. Based on this low melting point, the intersection of the liquid-graphite and liquid-cementite solubility lines was predicted to be 11°C below the iron-graphite eutectic temperature.

Due to experimental difficulties in the production of pure Fe_3C as a bulk sample and with the high temperature decomposition of this metastable phase, an experimental measurement of the melting point of Fe_3C has not been made. This investigation has shown that the stable to metastable transformation occurs at approximately 8°C below the iron-graphite eutectic temperature and this has fixed the intersection of the two solubility lines at a location which is in good agreement with Hillert's(18, 21) predictions. In combination with the eutectic points, the experimentally determined intersection of the solubility lines can be used to indicate the slope of the liquid - Fe_3C solubility curve and to fix the melting point of Fe_3C. The occurence of the metastable to stable transformation at a rate of approximately 40 mm/h corresponding to a undercooling of 5°C below the metastable Fe-Fe_3C eutectic temperature is further confirmatory evidence for the low melting point of Fe_3C.

7.7 Test of the Zener-Hillert Model

The results outlined above have led to a qualitative understanding of eutectic solidification in the iron-carbon systems. It remains to be seen whether the results agree in a quantitative manner with predictions of the Zener-Hillert theory.

To make this test, the interfacial tensions, $\sigma_{\alpha\beta}$, will be calculated for the two systems from the theoretical equations of the Zener-Hillert analysis (Section 2.2.2) using the Tiller (Section 2.2.3) minimum undercooling stability criterion. Equation (7) can be written

$$\frac{R}{D} = \beta \, \Delta T \, \frac{1}{\lambda}\left(1 - \frac{\lambda_c}{\lambda}\right) \tag{7}$$

where

$$\beta = \frac{1}{a} D \frac{\lambda^2}{\lambda_\alpha \lambda_\beta} \frac{\left(\frac{1}{m_\beta} - \frac{1}{m_\alpha}\right)}{(C^\beta - C^\alpha)} \tag{39}$$

The quantity, λ_c, can be evaluated from free energy considerations as in the Tiller analysis (Equations 13, 14 and 15). The free energy per unit volume, ΔF_v, can be estimated as

$$-\Delta F_v = \frac{\Delta H_v \Delta T}{T_E} - \frac{2\sigma_{\alpha\beta}}{\lambda} \quad . \tag{40}$$

Since the velocity and free energy difference vanish together where $\lambda = \lambda_c$,

$$\lambda_c = \frac{2\sigma_{\alpha\beta} T_E}{\Delta H_v \Delta T} \quad . \tag{41}$$

Substitution of Equ. (41) into Equ. (7) gives

$$\Delta T = \frac{R\lambda}{D\beta} + \frac{2\sigma_{\alpha\beta} \, T_E}{\lambda \Delta H_v} \quad . \tag{42}$$

Application of the minimum undercooling criterion yields

$$\sigma_{\alpha\beta} = \frac{R\lambda^2 \, \Delta H_v}{2 T_E D\beta} \tag{43}$$

Substitution of λ from Equ. (43) into Equ. (42) leads to

$$\sigma_{\alpha\beta} = \frac{(\Delta T)^2}{8R} \; \frac{\Delta H_v D\beta}{T_E} \qquad (44)$$

Experimental values from the two independent experiments can be substituted into Equ. (43) and (44) as a check on the internal consistency of the theory and on the reasonableness of the surface tensions obtained.

The numerical parameters used are as follows:

	Fe-C System	Fe-Fe$_3$C System
R =	110 mm/h	110 mm/h
λ =	6×10^{-5} cm (Fig. 33)	3×10^{-4} cm (Fig. 33)
a =	0.85	0.54
ΔH_v =	291 cal/cc(18)	300 cal/cc(18)
T_E =	1428°K	1423°K
D =	3×10^{-5} cm^2/sec	3×10^{-5} cm^2/sec
β =	0.0018	0.0408
ΔT =	8°C (Fig. 34)	9°C (Fig. 35)

The values for β were calculated from the phase diagram (Fig. 6) using values of "a" suggested by Hillert's(2) calculations. From Equations (43) and (44), $\sigma_{\alpha\beta}$ for the stable reaction was found to be 880 and 1200 ergs/cm^2 respectively. The corresponding values for the metastable reaction were 990 and 1115 ergs/cm^2, respectively.

These $\sigma_{\alpha\beta}$ values are of reasonable magnitude and the agreement of the results obtained from the independent measurements appear to be within the experimental errors and the errors implicit in this approximate theoretical analysis.

CHAPTER 8

SUGGESTIONS FOR FURTHER WORK

1. The solidification of cast iron with a nodular graphite morphology is of such practical importance that more work should be done along these lines in order to understand the mechanism of modification. Recent investigations have produced a better understanding of the factors involved but a novel approach is essential. One possible avenue is the use of transparent organic eutectic systems which solidify like metals in order to make direct observations of the solidification process. Jackson(97) has observed many of the features of eutectic growth which are characteristic of metals using these materials and it might be possible to find suitable additives which produce spheroids in these systems.

2. Of more theoretical interest is a more detailed investigation of the undercooling in the iron-carbon systems as a function of rate. Samples could be solidified either of two ways. Firstly, solidification in a steep temperature gradient with forced convection or, secondly, solidification in a low gradient with no convective mixing would accentuate inflections in the temperature profiles and increase the accuracy of the results. A very careful investigation of the Fe-Fe_3C system which exhibits the $R^{-1/3}$ relationship between solidification rate and spacing might be fruitful.

3. A more penetrating theoretical description is needed to explain the experimental observations.

4. A direct measurement of the melting point of Fe_3C would be of interest if experimental difficulties could be overcome.

CHAPTER 9

CONCLUSIONS

1. In Fe-C, Fe-C-Si, and Ni-C eutectic alloys, increasing solidification rates result in a modification of the morphology from regular lamellar to lacy to discontinuous.

2. An adsorption model for flake and nodular graphite growth which explains the experimental observations has been proposed. Changes in surface free-energy are of secondary importance.

3. Transmission electron microscopy has been used to elucidate the crystallographic growth habit of graphite nodules.

4. An $R^{-1/2}$ and an $R^{-1/3}$ relationship between interlamellar spacing and solidification rate have been observed in the two iron-carbon systems under identical conditions which cast doubt on the early theories of lamellar eutectic growth.

5. The undercooling at the solid-liquid interface has been measured in both systems and has been found to be consistent with a parabolic relationship as a function of growth rate.

6. The anticipated stable to metastable and metastable to stable transformations with increasing and decreasing rates respectively have been observed in the iron-carbon systems.

REFERENCES

1. Tiller, W. A., Liquid Metals and Solidification, American Society for Metals, Cleveland, 1958, p. 276.
2. Hillert, M., Jernkont. Ann., 141, 757 (1957).
3. Jackson, K. A., Chadwick, G. A., and Klugert, A., AIME Trans., 230, 1547 (1964).
4. Tiller, W. A., ASM Cast Iron Seminar, Detroit (1964).
5. Chadwick, G. A., Prog. Mat. Science, 12, 118 (1963).
6. Yue, A. S., AIME Trans., 224, 1010 (1962).
7. Zener, C., AIME Trans., 167, 550 (1946).
8. Tiller, W. A., J. Appl. Phys., 34, 3615 (1963).
9. Li, C. and Weart, H. W., unpublished work.
10. Kirkaldy, J. S., Decomposition of Austenite by Diffusional Processes, Interscience Publications, New York, 1962, p. 96 and p. 128.
11. Weart, H. W. and Mack, J. D., AIME Trans., 212, 664 (1958).
12. Rutter, W. J., Liquid Metals and Solidification, American Society for Metals, Cleveland, 1958, p. 243.
13. Yue, A. S., J.I.M., 92, 248 (1963-4).
14. Bell, J. A. E., Ph.D. Thesis, University of Toronto (1965).
15. A.S.M. Metals Handbook, ASM, Cleveland, 1948.
16. Hansen, M., Constitution of Binary Alloys, McGraw-Hill, New York, 1958.
17. Kirkaldy, J. S., Aspects of Modern Ferrous Metallurgy, University of Toronto Press, Toronto, 1963, p. 263.

18. Hillert, M., ASM Cast Iron Seminar, Detroit (1964).

19. Darken, L. S., and Gurry, R. W., Physical Chemistry of Metals, McGraw-Hill, New York, 1953, p. 401.

20. Handbook of Chemistry and Physics, 40th edition, Chemical Rubber Publishing Co., Cleveland, Ohio (1958).

21. Hillert, M., Acta Met., 3, 37 (1955).

22. Morrogh, H. and Williams, W. J., J.I.S.T., 155, 321 (1947).

23. Hughes, I. C. H., J. Aust. I. M., 10, 4 (1965).

24. Rickard, J. and Hughes, I. C. H., BCIRA Journ., 9, 11 (1961).

25. Hillert, M. and Steinhäuser, H., Jernkont. Ann. 144, 520 (1960).

26. Wilkinson, M. P. and Hellawell, A.,BCIRA Journ., 11, 439 (1963).

27. Brigham, R. J., Purdy, G. R., and Kirkaldy, J. S., Can. Met. Quart., 3, 239 (1964).

28. Bunin, K. P., Malinochka, Ya. N., and Fedorova, S. A., Liteinoe Proiz vodstvo, 4, 25 (1953). (BCIRA Translation No. 677).

29. Morrogh, H., and Oldfield, W., Iron and Steel, 32, 431 and 479 (1959).

30. Merchant, H. D., Foundry, 89, 80 (1961).

31. Oldfield, W., BCIRA Jour., 8, 177 (1960).

32. Morrogh, H., British Foundryman, 53, 221 (1960).

33. Morrogh, H, , Mod. Castings, 42, 37 (1962).

34. Loper, C. R., and Heine, R. W., Mod. Castings, 40, 117 (1961).

35. Koves, G., and Mondolfs, L. F., J.I.S.I., 202, 424 (1964).

36. Lakeland, K. D., British Foundryman, 56, 508 (1963).

37. Lakeland, K.D., BCIRA Jour., 12, 634 (1964).

38. Boyes, J. W., and Fuller, A. G., BCIRA Jour., 12, 424 (1964).

39. Boyes, J. W., BCIRA Jour., 10, 9 (1962).
40. ibid , 11, 13 (1963).
41. ibid , 9, 499 (1961).
42. Ensor, T., unpublished work at BCIRA.
43. Fuller, A. G., BCIRA Jour., 11, 111 (1963).
44. Boyes, J. W., BCIRA Jour., 11, 336 (1963).
45. ibid , 10, 568 (1962).
46. Oldfield, W., BCIRA Jour., 9, 506 (1961).
47. ibid , 10, 17 (1962).
48. Lux, B.,and Tannenberger, H., Mod. Castings, 41, 57 (1962).
49. Fuller, A. G., BCIRA Jour., 9, 693 (1961).
50. Dawson, J. V., BCIRA Jour., 9, 199 (1961).
51. Hughes, I. C. H., and Oldfield, W., BCIRA Jour., 10, 475 (1962).
52. Hillert, M., ASM Trans., 53, 555 (1961).
53. Morrogh, H., and Williams, W. J., J.I.S.I., 158, 306 (1948).
54. Millis, K. D., Gagnebin, A. P., and Pilling, N. B., U.S. Patent 2485760. Application Date Nov. 21, 1947.
55. Oldfield, W., and Humphreys, J. G., BCIRA Jour., 10, 315 (1962).
56. Morrogh, H., British Foundryman, 53, 88 (1960).
57. Morrogh, H., J.I.S.I., 143, 195 (1941).
58. Stauss, H. E., Von Batchelder, F. W., and Salkovitz, E. I., J. of Metals, 3, 249 (1951).
59. Minkoff, I., Mod. Castings, 41, 66 (1962).
60. Kozakevitch, P., et al., Rev. Met., 52, 139 (1955).
61. Sidorenko, R. A. and Tsarevskii, B. V., Phys. Metals and Metallography, 10(6), 73 (1960).

62. Khranov, A. Ia. and Chernobrovkin, V. P., Phys. Metals and Metallography, 4(2), 149 (1957).

63. Lyubchenko, A. P., et al, Phys. Metals and Metallography, 12(2), 63 (1961).

64. Hillert, M. and Lindblom, Y., J.I.S.I., 176, 388 (1954).

65. Khrapov, A. Ia., Phys. Metals and Metallography, 6(2), 92 (1958).

66. Schadler, H. W., The Art and Science of Growing Crystals (J. J. Gilman ed.), John Wiley and Sons, New York, 1963, p. 343.

67. Calverley, A., Davis, M. and Lever, R. F., J. Sci. Inst., 34, 142 (1957).

68. Rocco, W. A., and Sears, G. W., J. Sci. Inst., 27, 1 (1956).

69. Strong, H. M., AIME Trans., 233, 643 (1965).

70. Chadwick, G. A., J.I.M., 92, 18 (1963-64).

71. Tiller, W. A., and Mrdjenovich, R., J. Appl. Phys., 34, 3639 (1963).

72. Tiller, W. A., ASM Seminar on Cast Iron, Detroit (1964).

73. Whelan, E. P., Private Communication.

74. Hunt, J. D., and Chilton, J. P., J.I.M., 92, 21 (1963-4).

75. Scheil, E., Z. Metallkunde, 37, 1 (1946).
Z. Metallkunde, 45, 298 (1954).
Giesserei , 24, 1313 (1959).

76. Hillert, M., J.I.S.I., 178, 158 (1954).

77. Oron, M., and Minkoff, I., Phil. Mag., 9, 1059 (1964).
A.S.M. Cast Iron Seminar, Detroit, (1964).

78. Ballinger, J., Hughes, I.C.H., and Mulvey, T., B.C.I.R.A. Jour. 8, 232 (1960).

79. Merchant, H. D., Toriello, L. I., and Wallace, J. F., Mod. Castings, 39, 109 (May 1961).

80. Patterson, W., and Ammann, D., Giesserei Tech-Wiss. Beihefte, 13, 65 (1961).

81. Bolstov, I. E. et al, Phys. Metals and Metallography, 4(1), 144 (1957).

82. Barton, R., B.C.I.R.A. Jour., 11, 741 (1963).

83. Loper, C. R., Kim, C. B., Htun, K. M., and Heine, R. W., ASM Cast Iron Seminar, Detroit (1964).

84. Gorskkov, A. A., Lit. proizvod., 3, 17 (1955).

85. Scheil, E., Z. Metallk., 40, 246 (1949).

86. Coates, R. B., and Leyshon, H. J., B.C.I.R.A. Jour., 12, 507 (1964).

87. Ward, R. G. and Sharma, S. K., to be published in J.I.S.I.

88. Lakeland, K. D., J. Aust. I. M., 10, 55 (1965).

89. Ward, R. G., The Physical Chemistry of Iron and Steel Making, Edward Arnold (Publishers) Ltd., London, 1962, p. 109.

90. Ward, R. G. and Hall, R., J.I.S.I., 195, 75 (1960).

91. Shapiro, J. M., Private Communication.

92. Cooksey, D. J. S., Munson, D., Wilkinson, M. P., and Hellawell, A., Phil. Mag., 10, 745 (1964).

93. Von Rosenstiel, A. P. and Bakkerus,H., Giesserei Techn-Wiss. Beihefte, 16, 149 (1964).

94. Von Rosenstiel, A. P., Mikrochemica Acta, 3, 525 (1965).

95. Zeedijk, H. B., J.I.S.I., 203, 737 (1965).

96. Kirkaldy, J. S., Private Communication.

97. Jackson, K. A., Private Communication.

TABLE I Chemical Analysis of Alloy B

S	Si	P	Mn	Cr	Cu	Sn	Ni
0.019	0.001	0.004	0.06	0.001	0.065	0.009	0.025

TABLE II Chemical Analysis of Alloy C

S	Si	P	Mn	Cr	Cu	Sn	Ni
0.008	<0.001	<0.001	<0.002	<0.0008	<0.002	<0.001	<0.004

TABLE III Chemical Analysis of Alloy Si

S	Si	P	Mn	Cr	Cu	Sn	Ni
.020	3.24	0.004	0.06	0.001	0.065	0.009	0.025

TABLE IV Table of Interlamellar Spacing Measurements

$Fe-Fe_3C$		Fe-C	
R mm/n	$\lambda \pm 1\sigma$ mm x 10^{-3}	R mm/n	$\lambda \pm 1\sigma$ mm x 10^{-3}
560	1.67 ± 0.05	91.7	0.63 ± 0.02
282	2.12 ± 0.13	19.6	1.58 ± 0.03
118	3.03 ± 0.12	5.0	3.77 ± 0.20
82.9	3.31 ± 0.08		
58.4	3.89 ± 0.27		

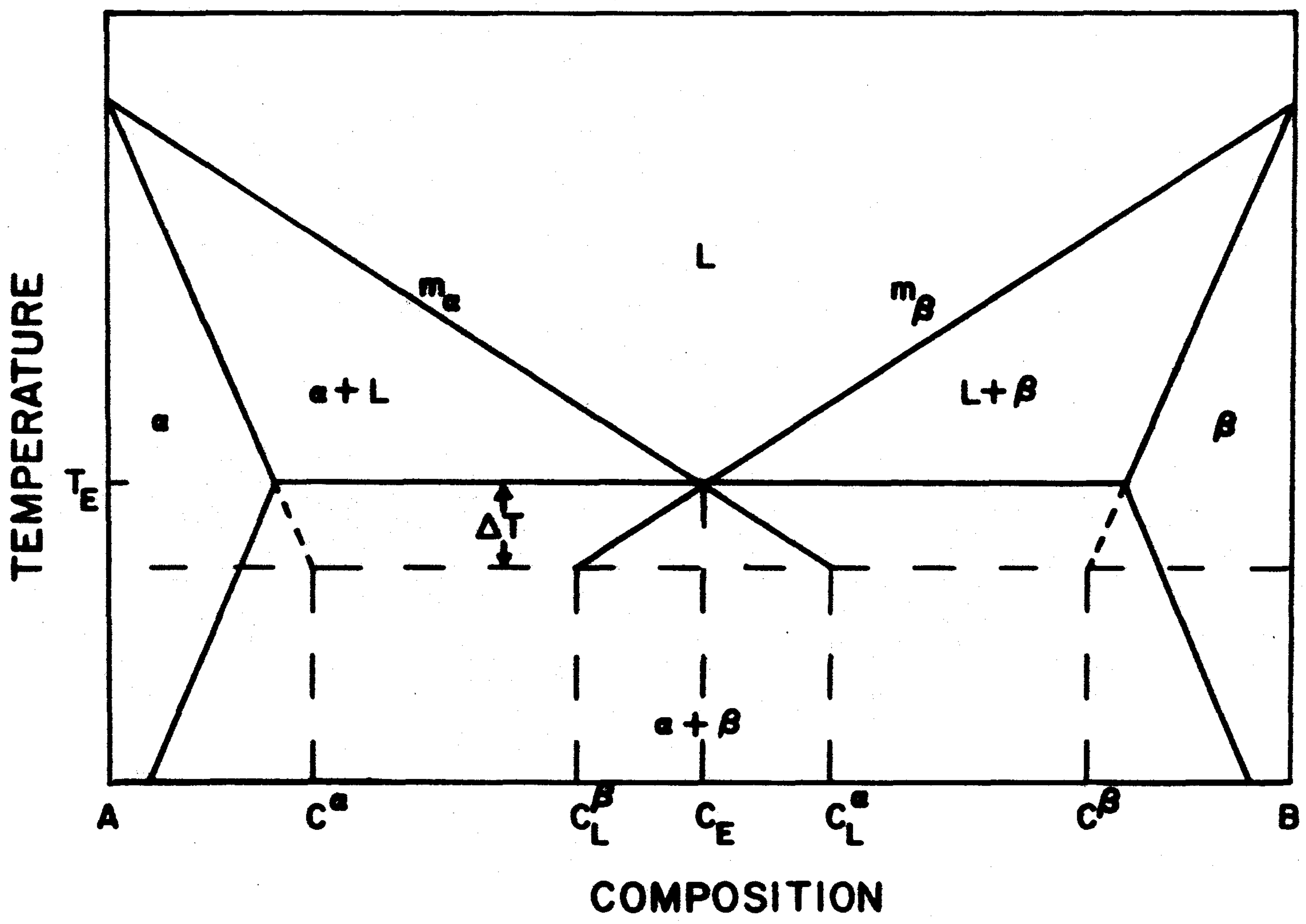

Figure 1 Schematic eutectic phase diagram.

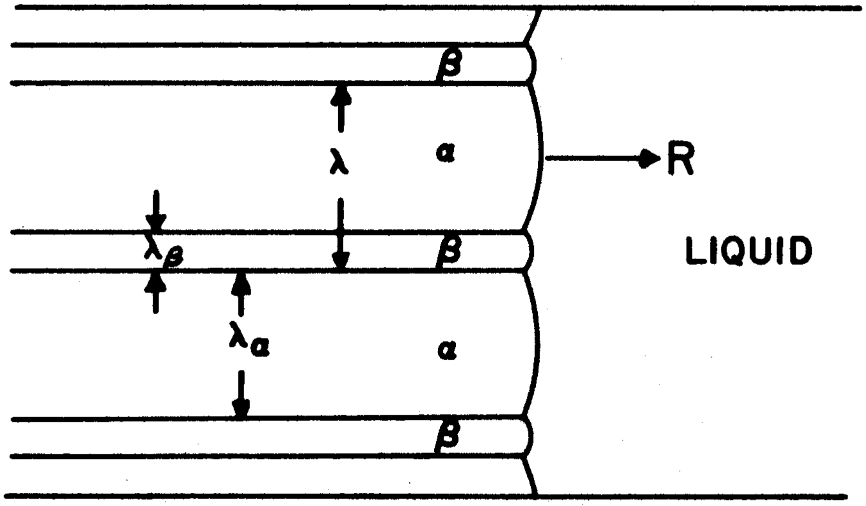

Figure 2 Schematic configuration of lamellar eutectic growth.

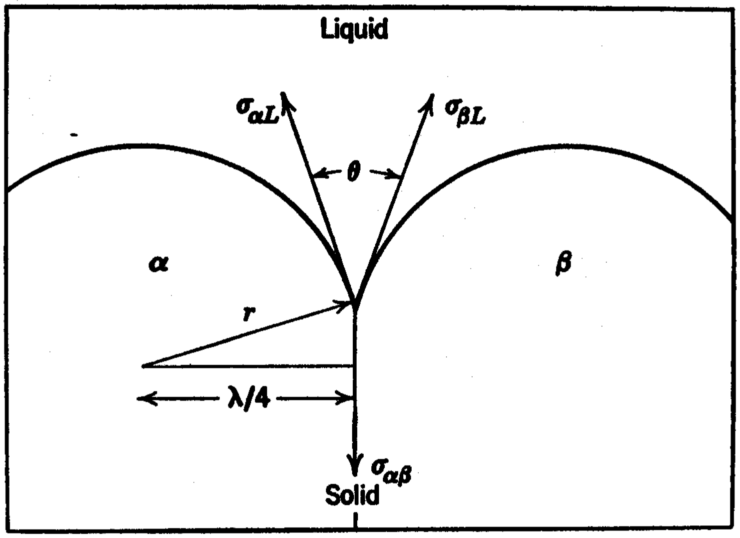

Figure 3 Schematic configuration of lamellar eutectic growth after Jackson and Chalmers(5).

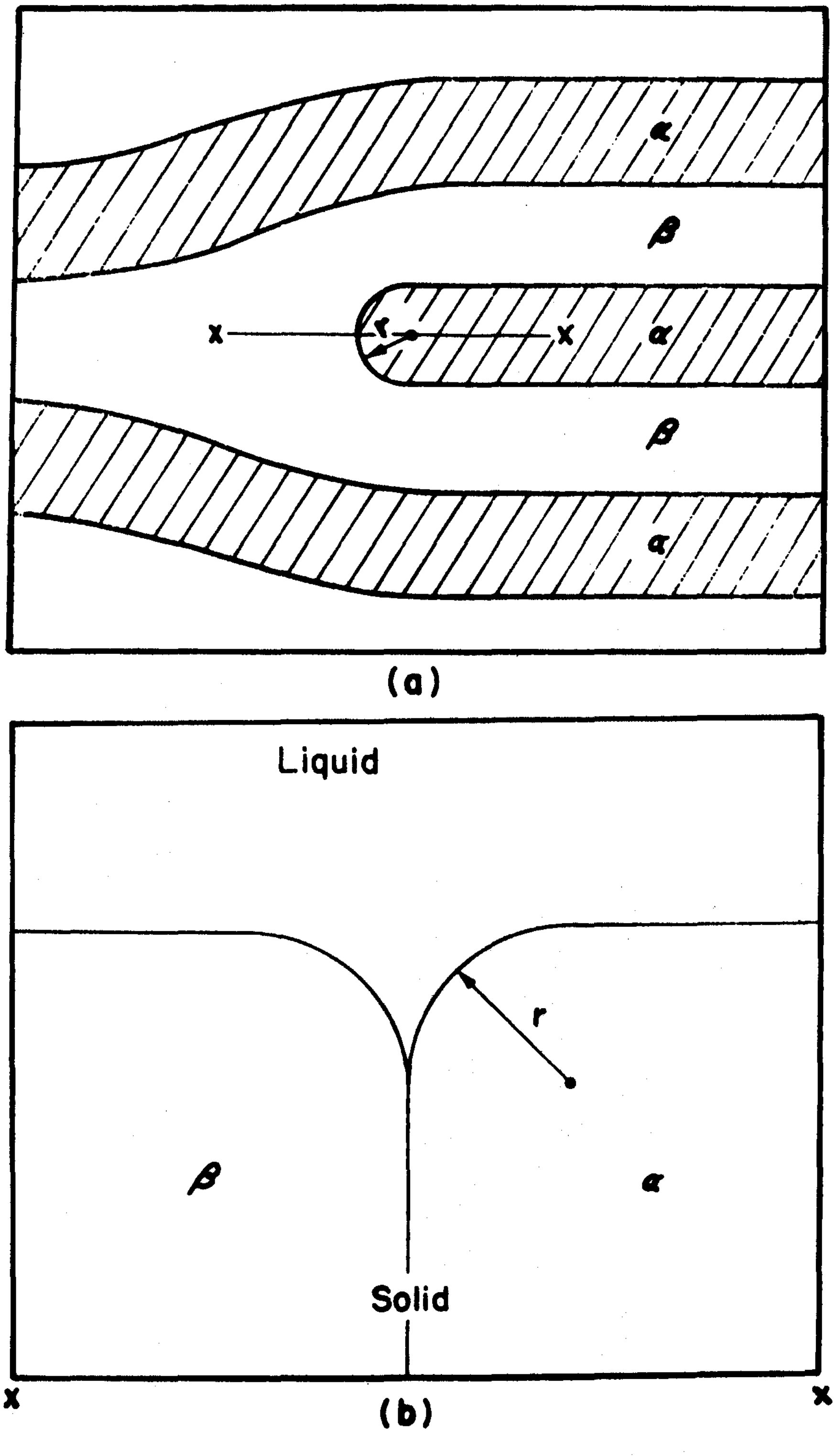

Figure 4 Schematic configuration of lamellar eutectic structure at a termination after Jackson and Chalmers(5).

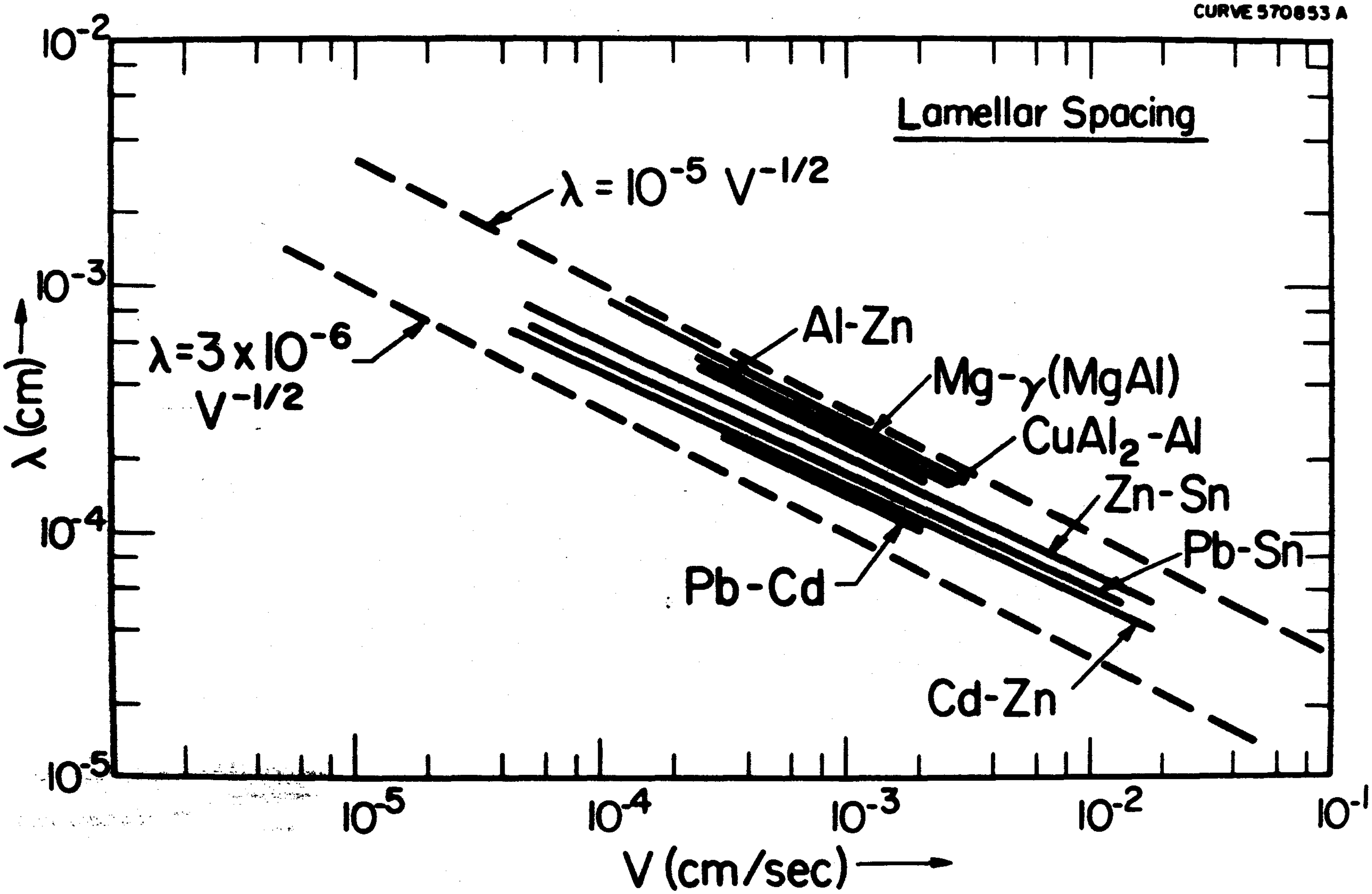

Figure 5 Plot of interlamellar spacing versus growth rate for several eutectic systems after Tiller(72).

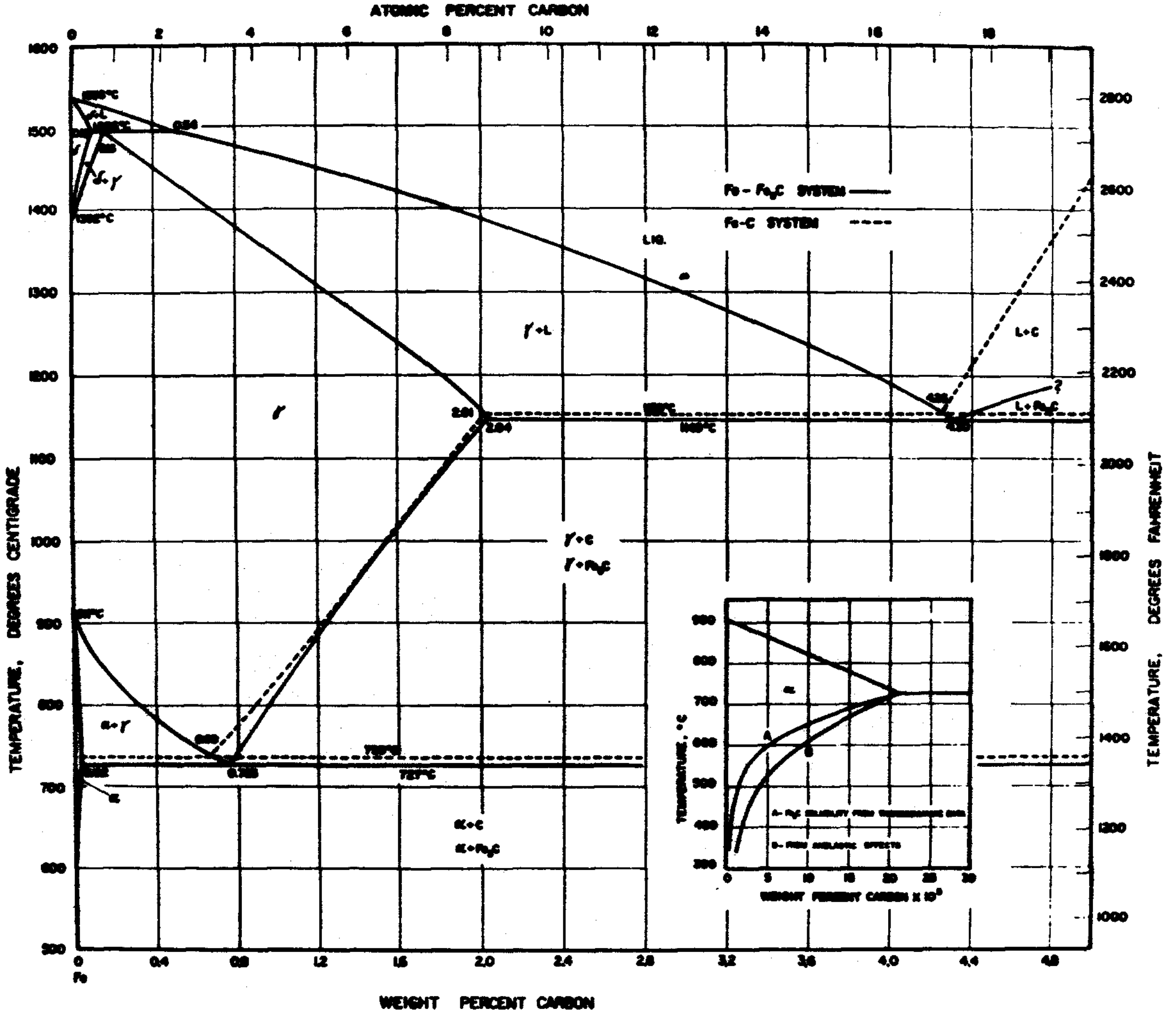

Figure 6 The iron-carbon constitution diagram after Kirkaldy and Purdy(17).

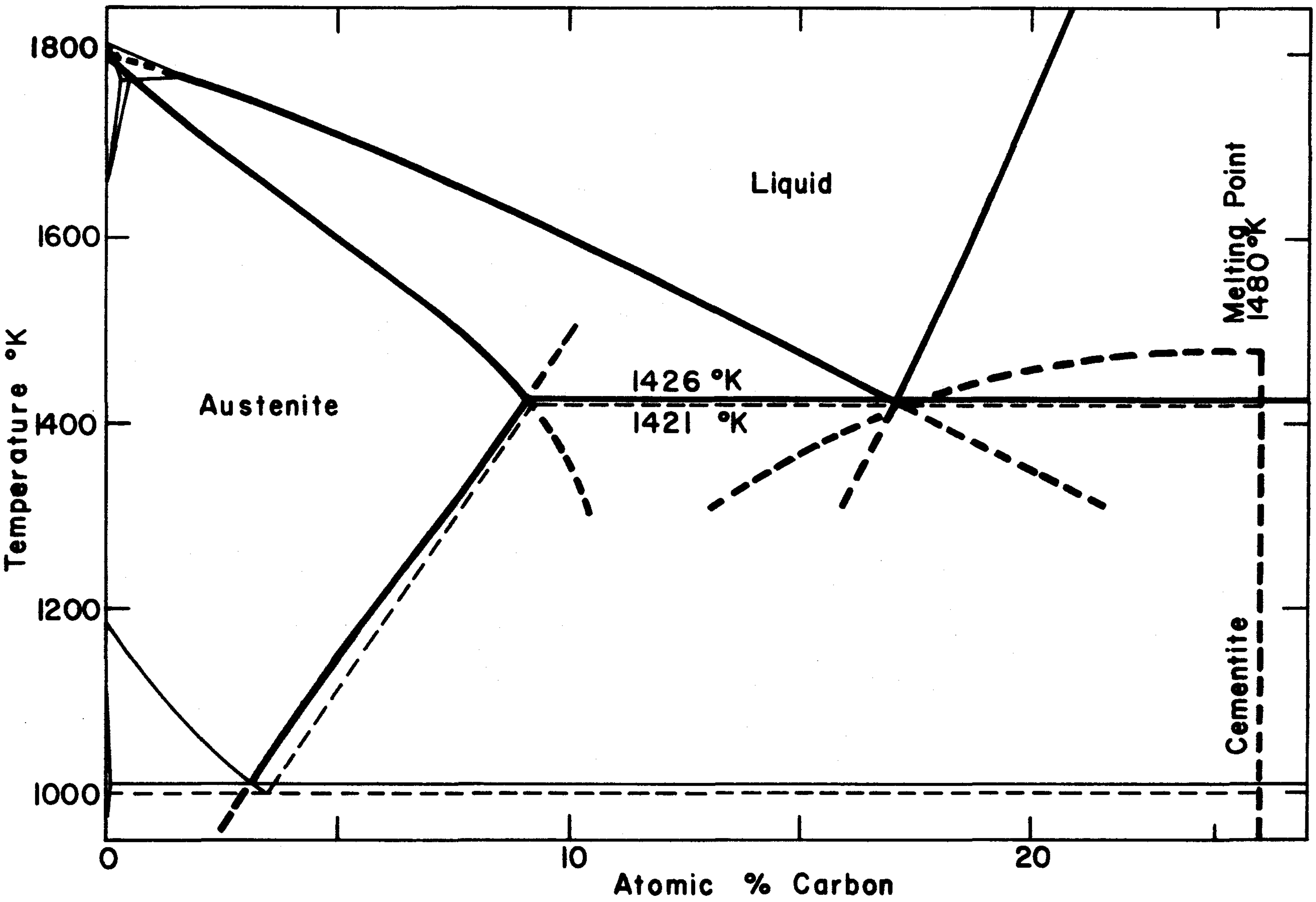

Figure 7 The iron-carbon constitution diagram after Hillert(18). The full lines represent the Fe-C system and the dashed lines the Fe-Fe_3C system. All thick lines, full and dashed, were calculated.

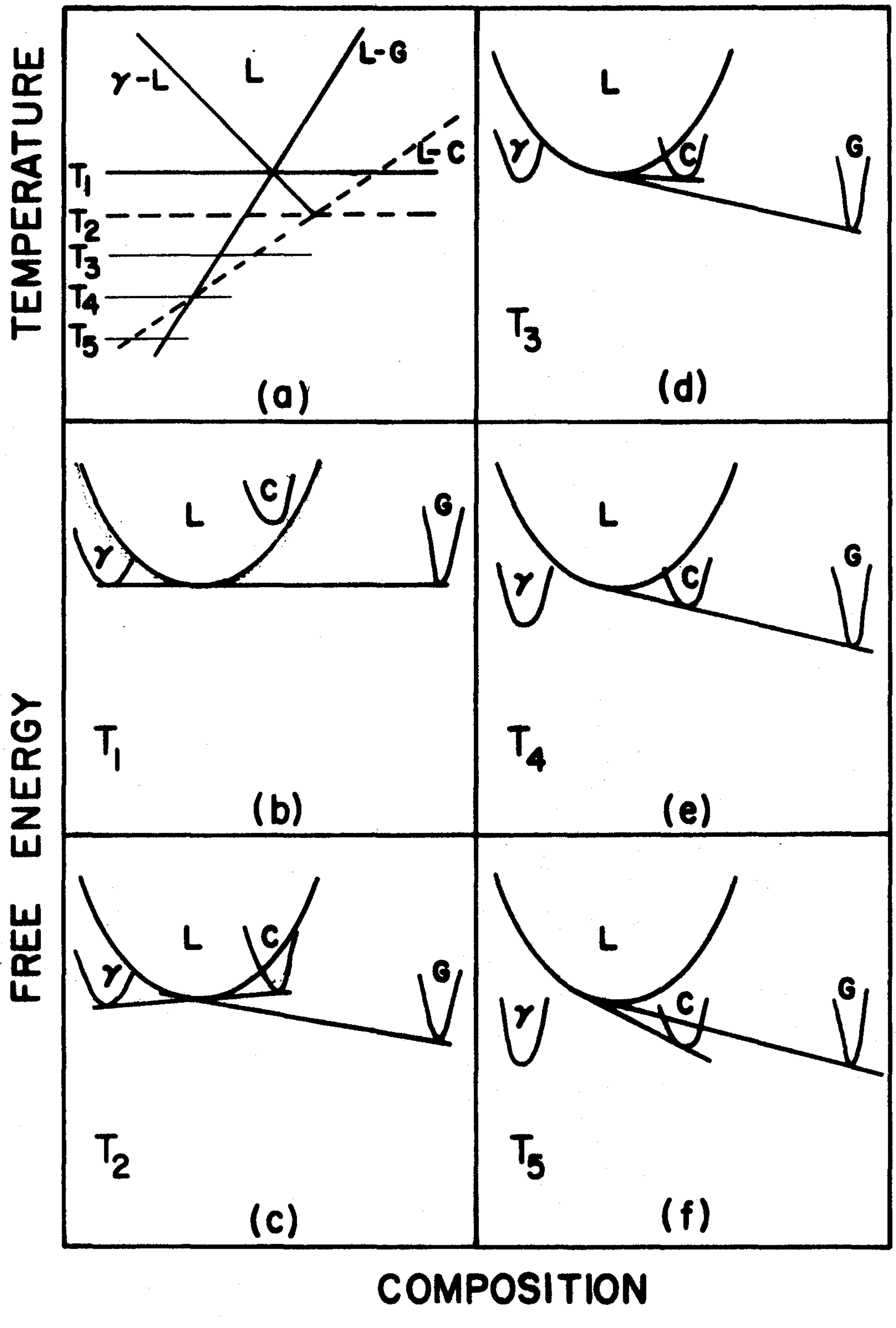

Figure 8 Free energy-composition diagrams of the iron-carbon system at various undercoolings.

Figure 9 Photomicrograph of plate-like cementite structure after Rickard and Hughes(24). (X100) (Picral etch)

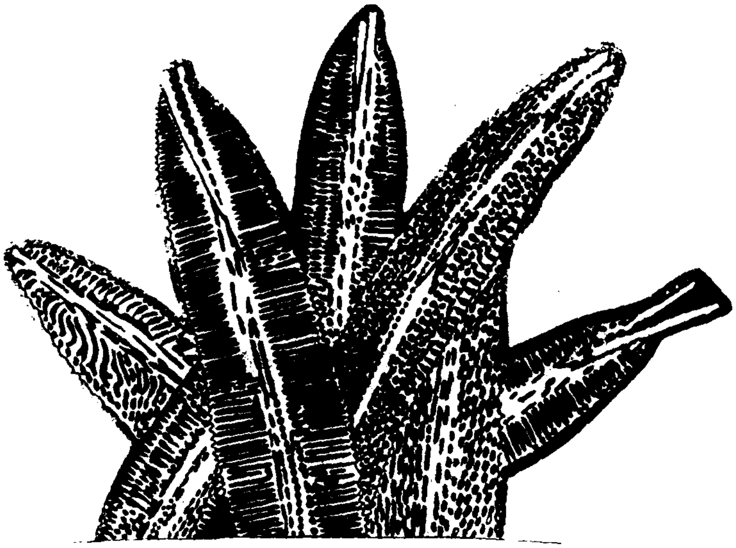

Figure 10 Artist's conception of growing ledeburite eutectic cells.

Figure 11 Artist's conception of the eutectic cell graphite structure.

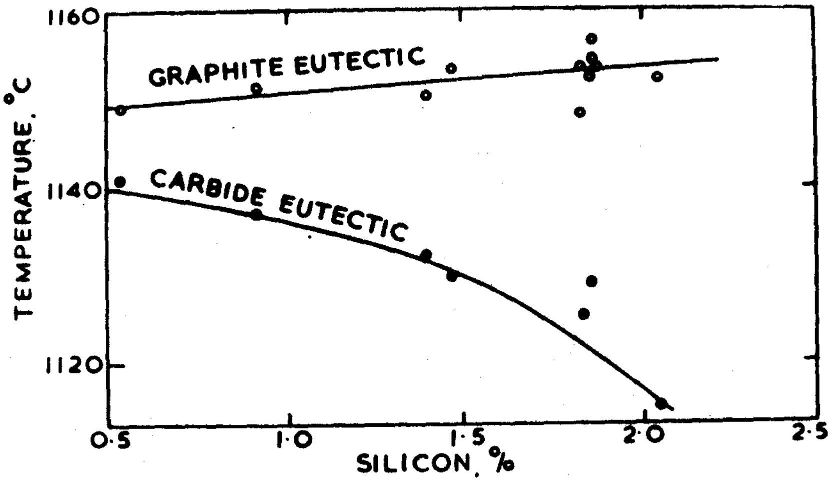

Figure 12 Effect of Si on the Fe-C and Fe-Fe_3C eutectic temperatures after Oldfield$^{(47)}$.

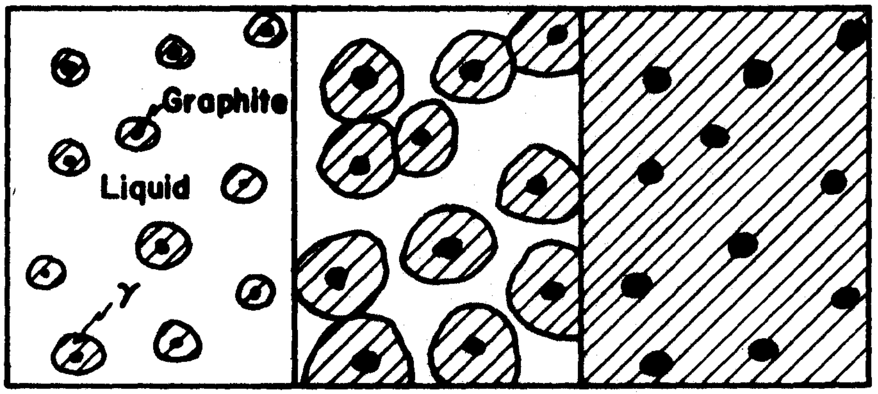

Figure 13 Schematic illustration of grow stages from liquid to nodular graphite eutectic.

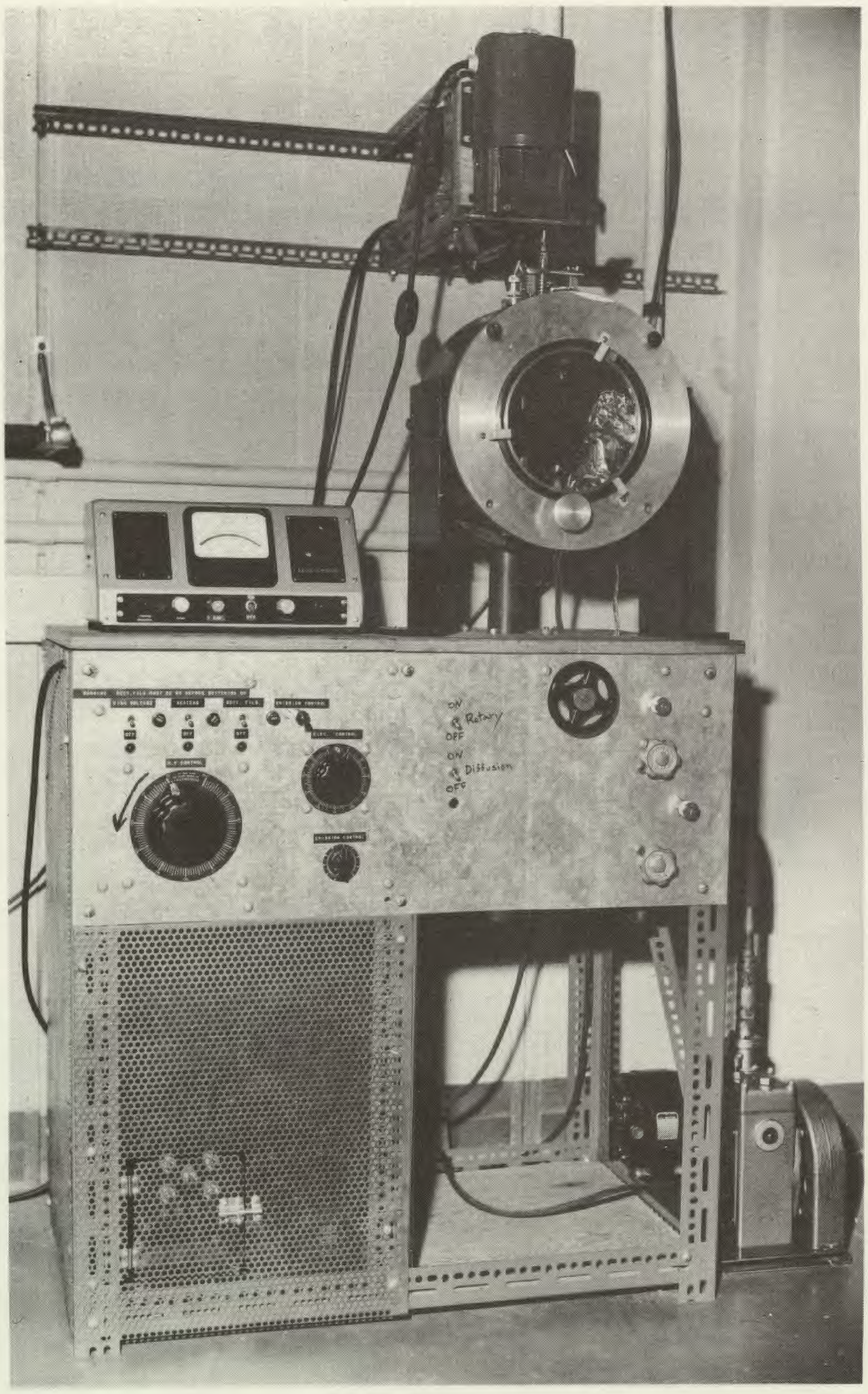

Figure 14 Photograph of the electron-beam melting apparatus.

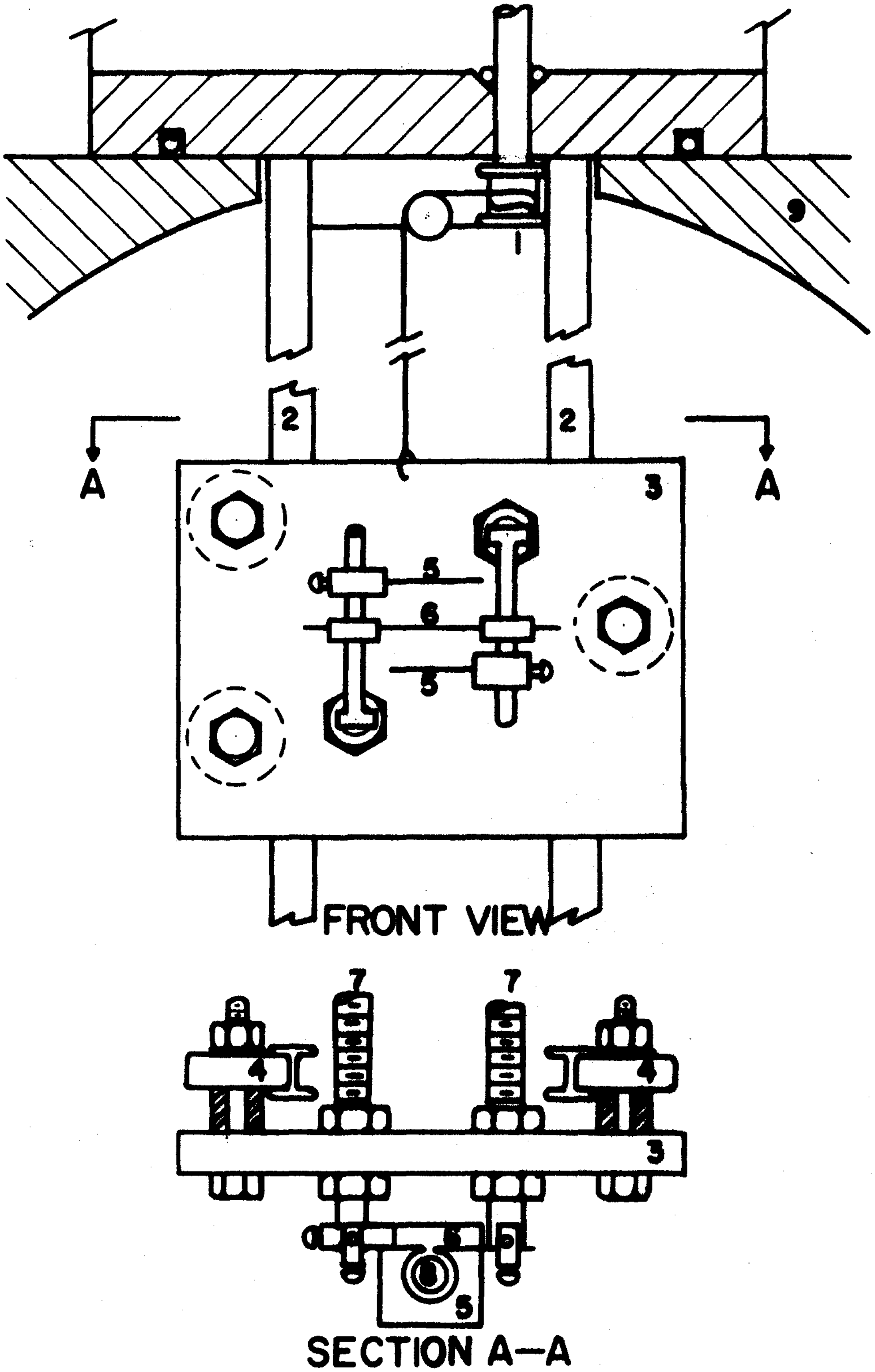

Figure 15 Electrode assembly in electron-beam melting apparatus.

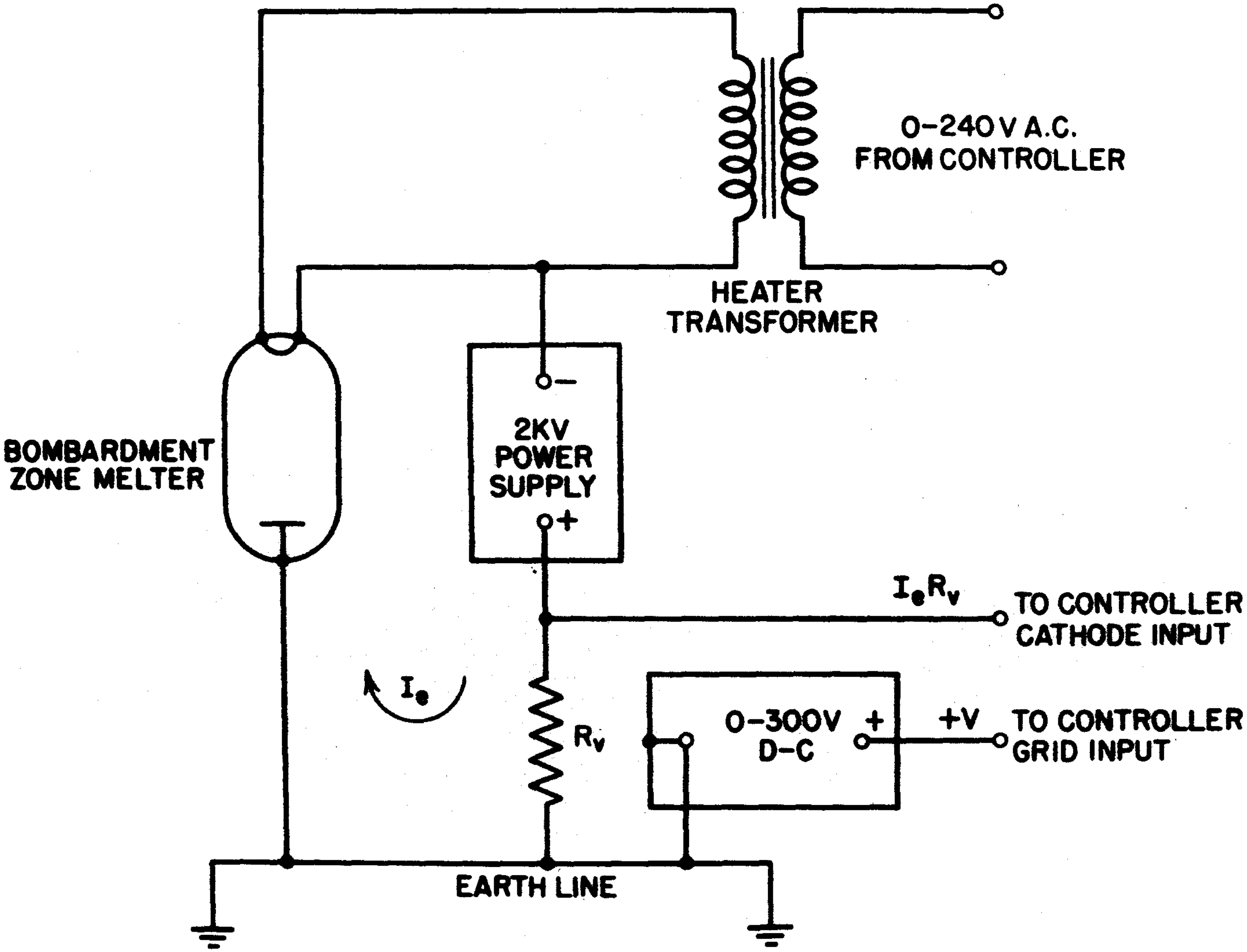

Figure 16 Block diagram of the electric circuit in the electron-beam melting apparatus after Calverley et al(67).

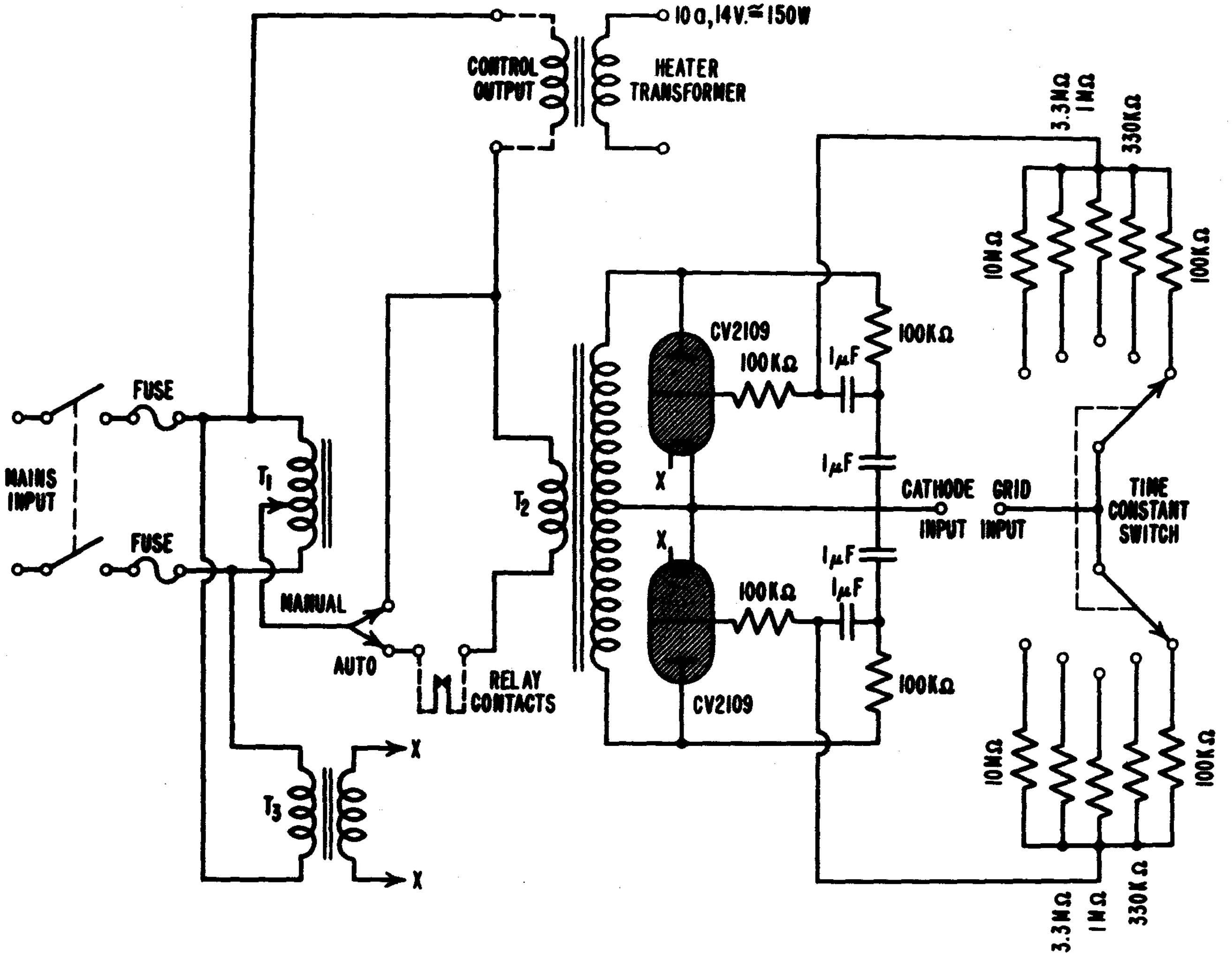

Figure 17 Thyratron control circuit after Calverley et al(67).

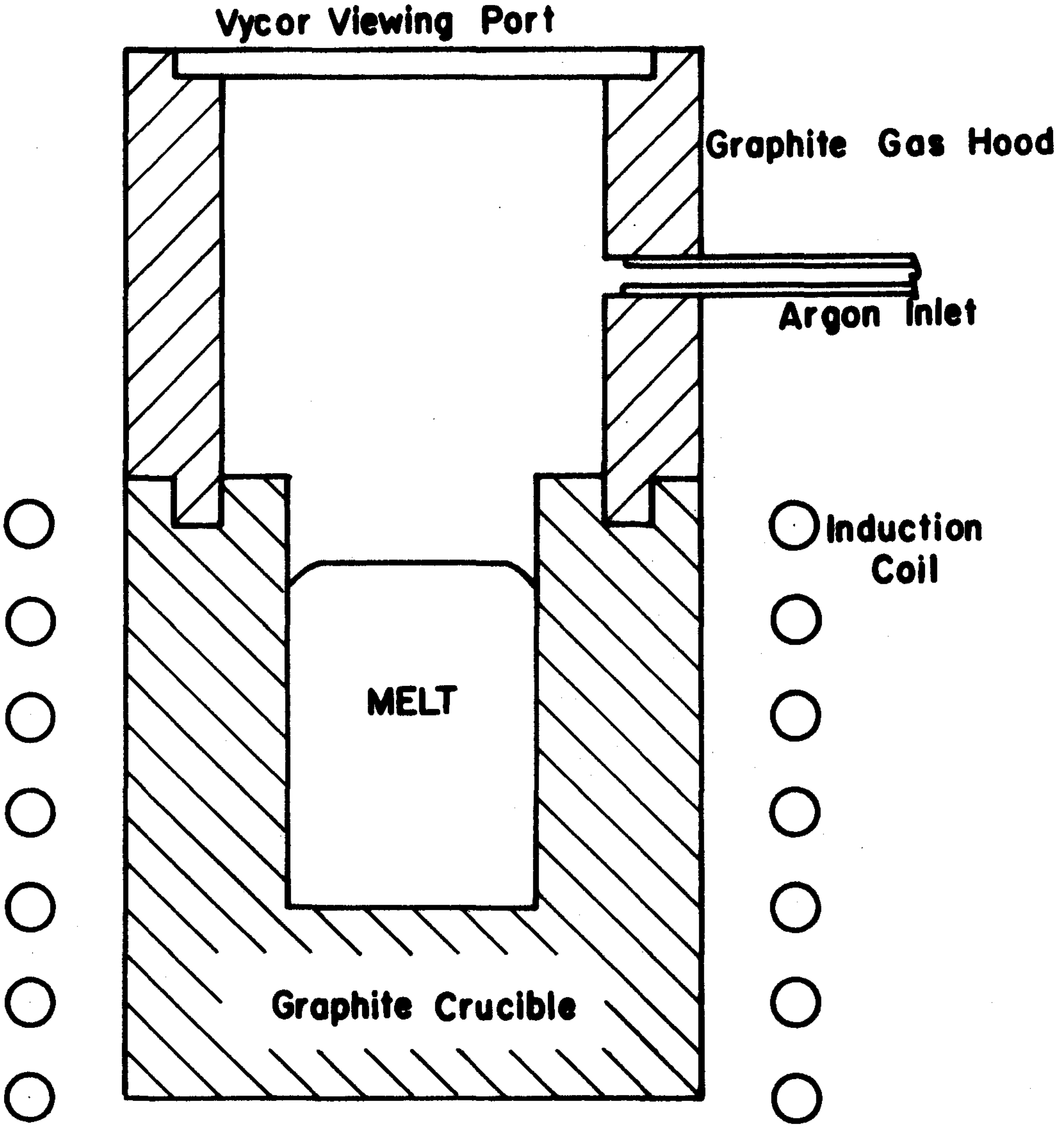

Figure 18 Melting Crucible showing gas hood and argon inlet.

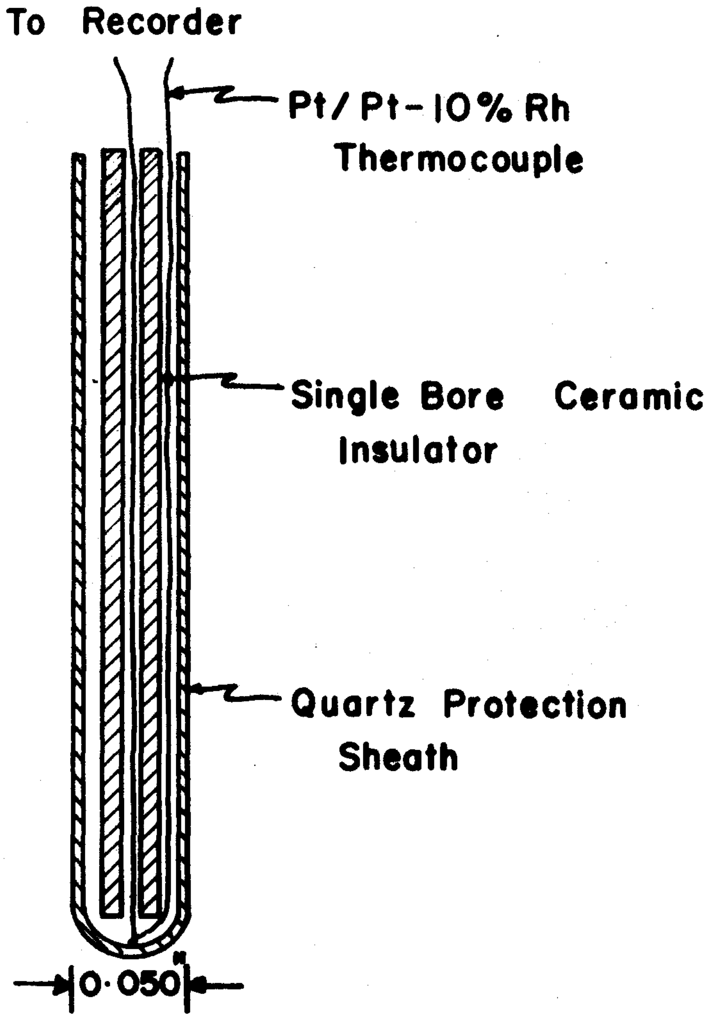

Figure 19 Minature thermocouple and protection sheath.

Figure 20 Micrograph of lamellar Fe-C alloy solidified at 2.0 mm/h. Arrow indicates the direction of solidification.(X83) (unetched)

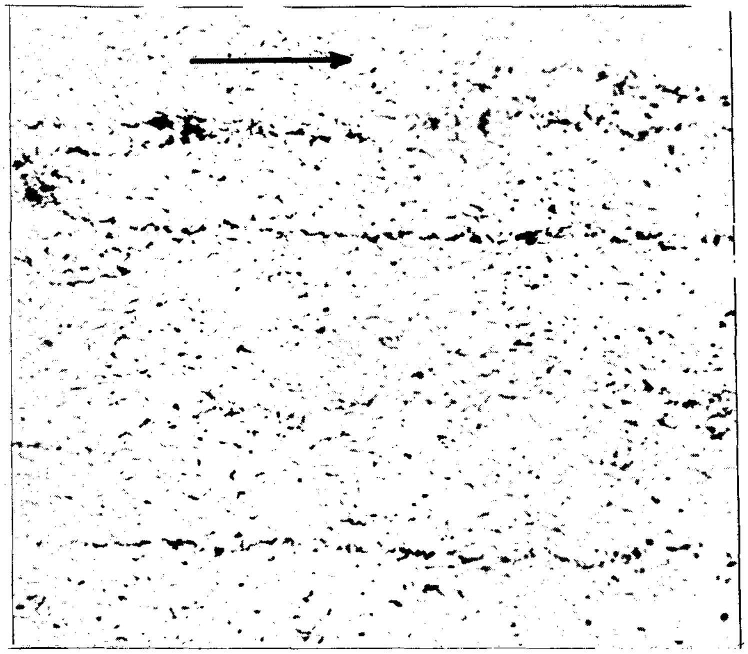

Figure 21 Micrograph of lacy Fe-C alloy solidified at 18.1 mm/h. Arrow indicates the direction of solidification.(X224) (unetched)

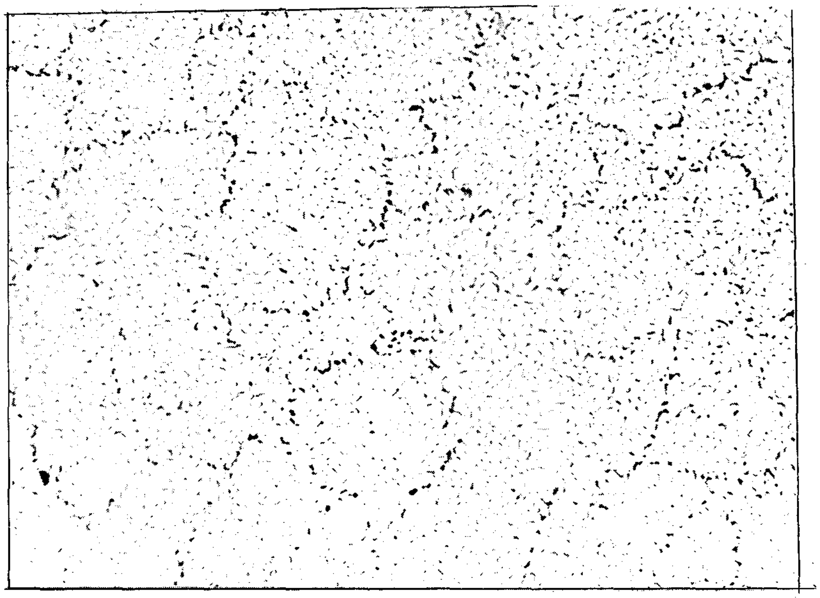

Figure 22 Micrograph of cross-section of Fe-C alloy solidified at 18.1 mm/h. (X224) (unetched)

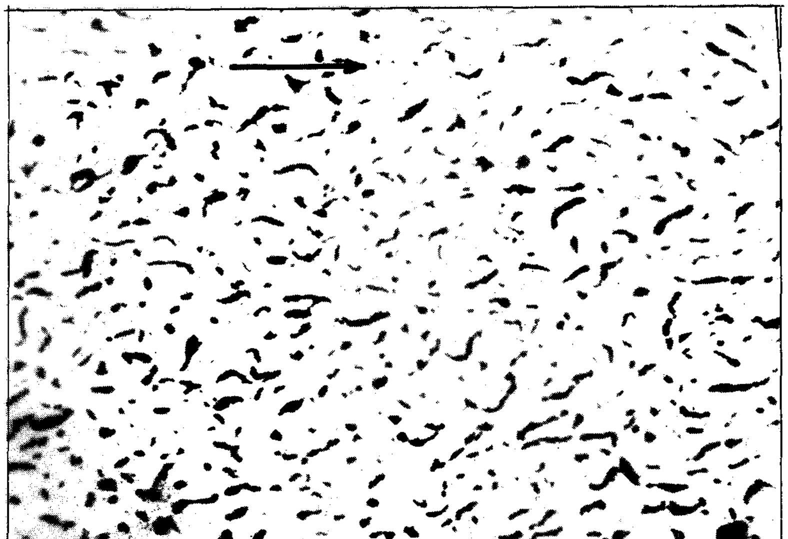

Figure 23 Micrograph of lacy Fe-C alloy solidified at 60.0 mm/h. Arrow indicates the direction of solidification. (X410) (unetched)

Figure 24 Micrograph of lamellar Fe-Fe_3C alloy solidified at 60.0 mm/h. Arrow indicates the direction of solidification. (X410) (Nital etch)

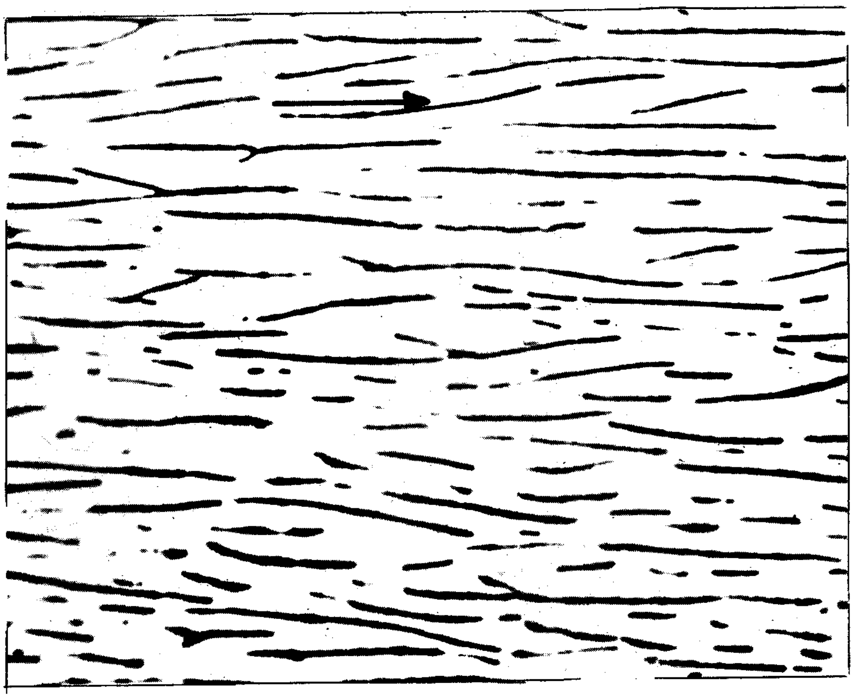

Figure 25 Micrograph of lamellar Ni-C alloy solidified at 24.0 mm/h. Arrow indicates the direction of solidification. (X340) (unetched)

Figure 26 Micrograph of lacy Ni-C alloy solidified at 180 mm/h. Arrow indicates the direction of solidification (X340) (unetched)

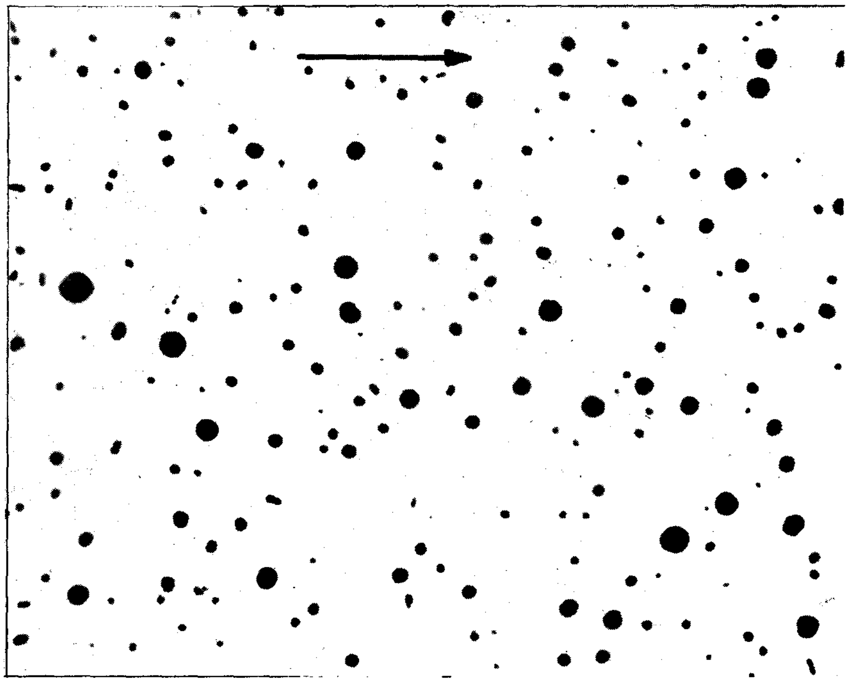

Figure 27 Micrograph of nodular Ni-C alloy solidified at 440 mm/h. Arrow indicates the direction of solidification. (X340) (unetched)

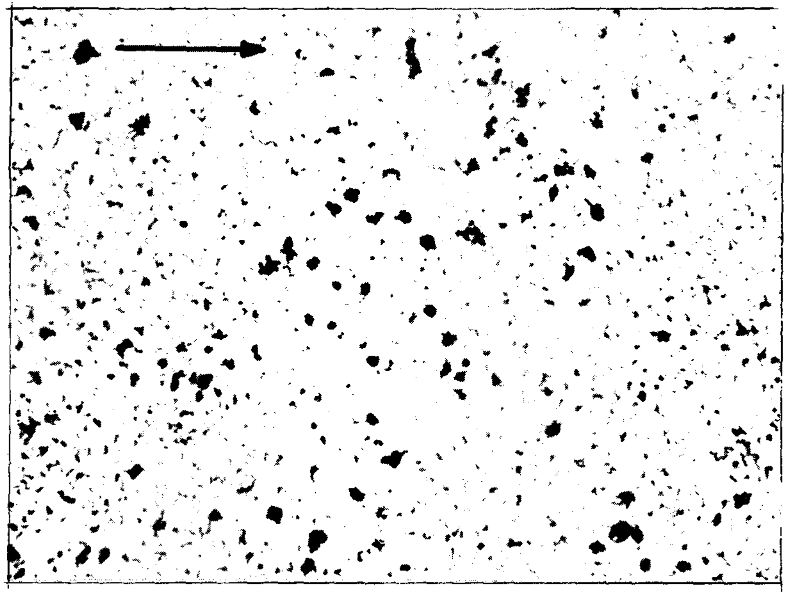

Figure 28 Micrograph of lacy Fe-C-Si alloy solidified at 670 mm/h. Arrow indicates the direction of solidification. (X460) (unetched)

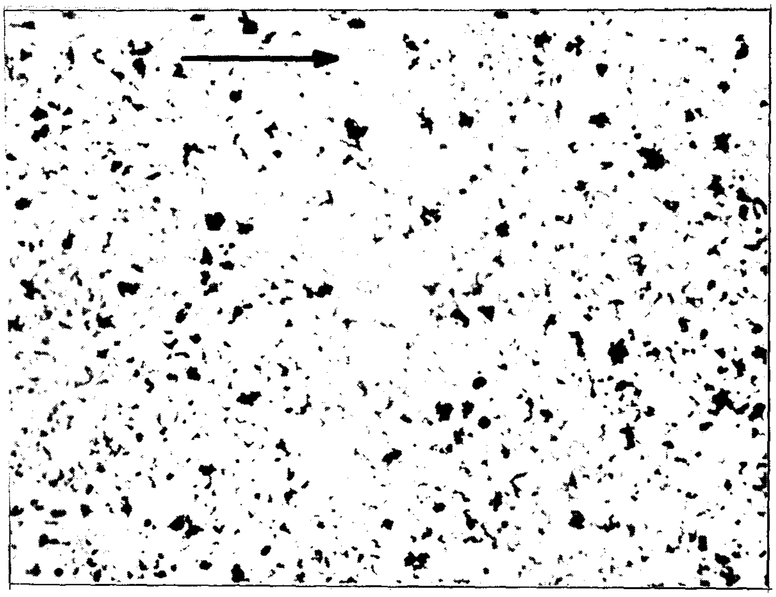

Figure 29 Micrograph of lacy Fe-C-Si alloy solidified at 860 mm/h. Arrow indicates the direction of solidification. (X460) (unetched)

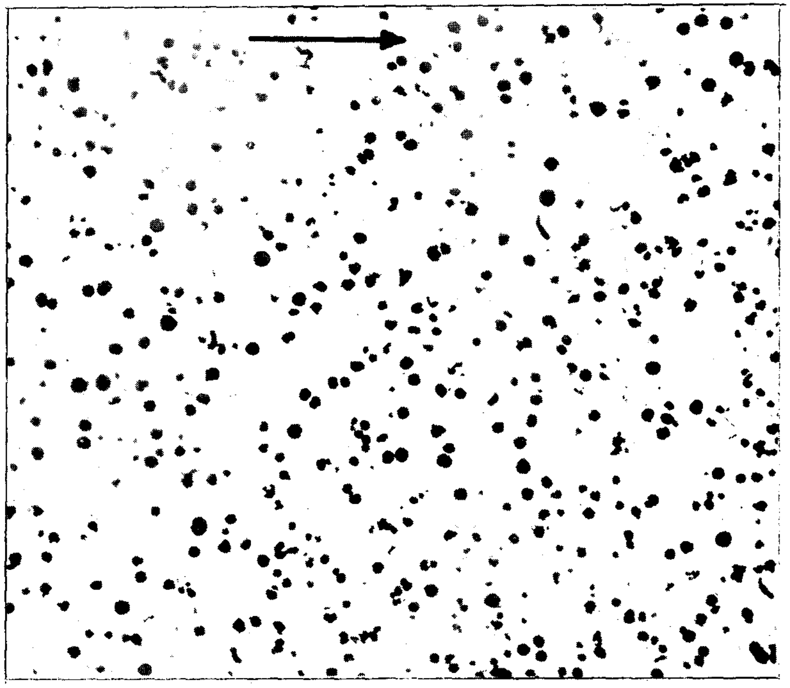

Figure 30 Micrograph of cerium-treated nodular Fe-C-Si alloy solidified at 500 mm/h. Arrow indicates the direction of solidification. (X224) (unetched)

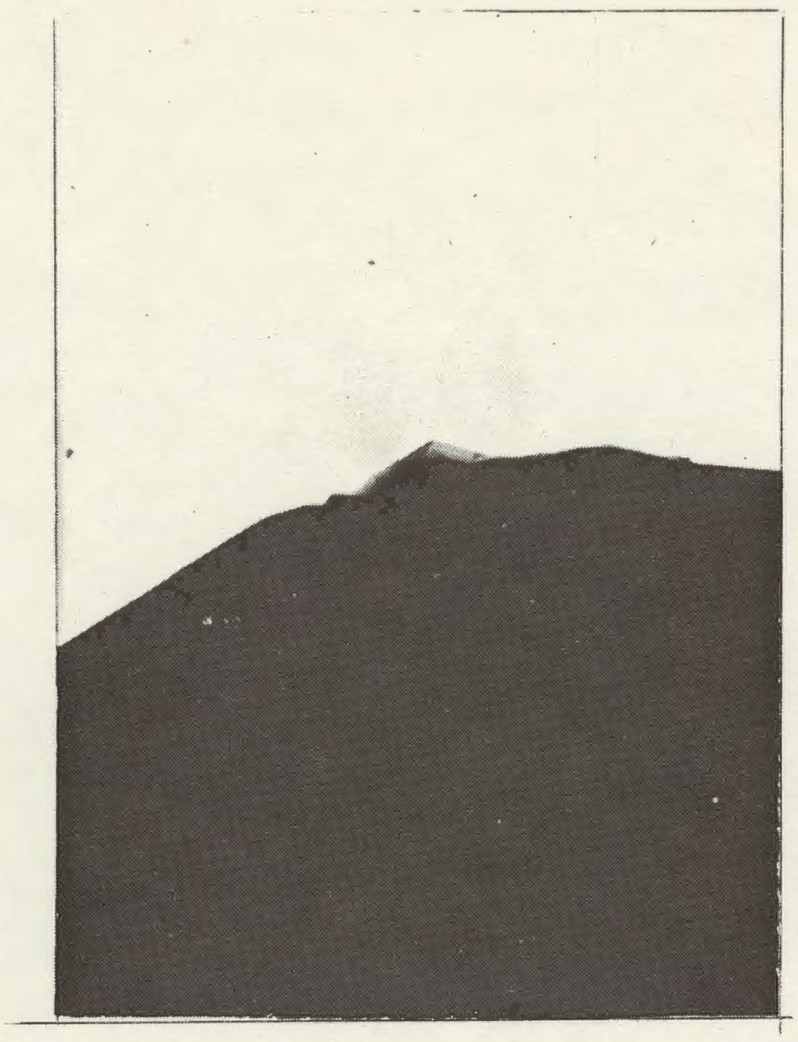

Figure 31 Electron micrograph of the surface of a graphite spheroid. (X20,000)

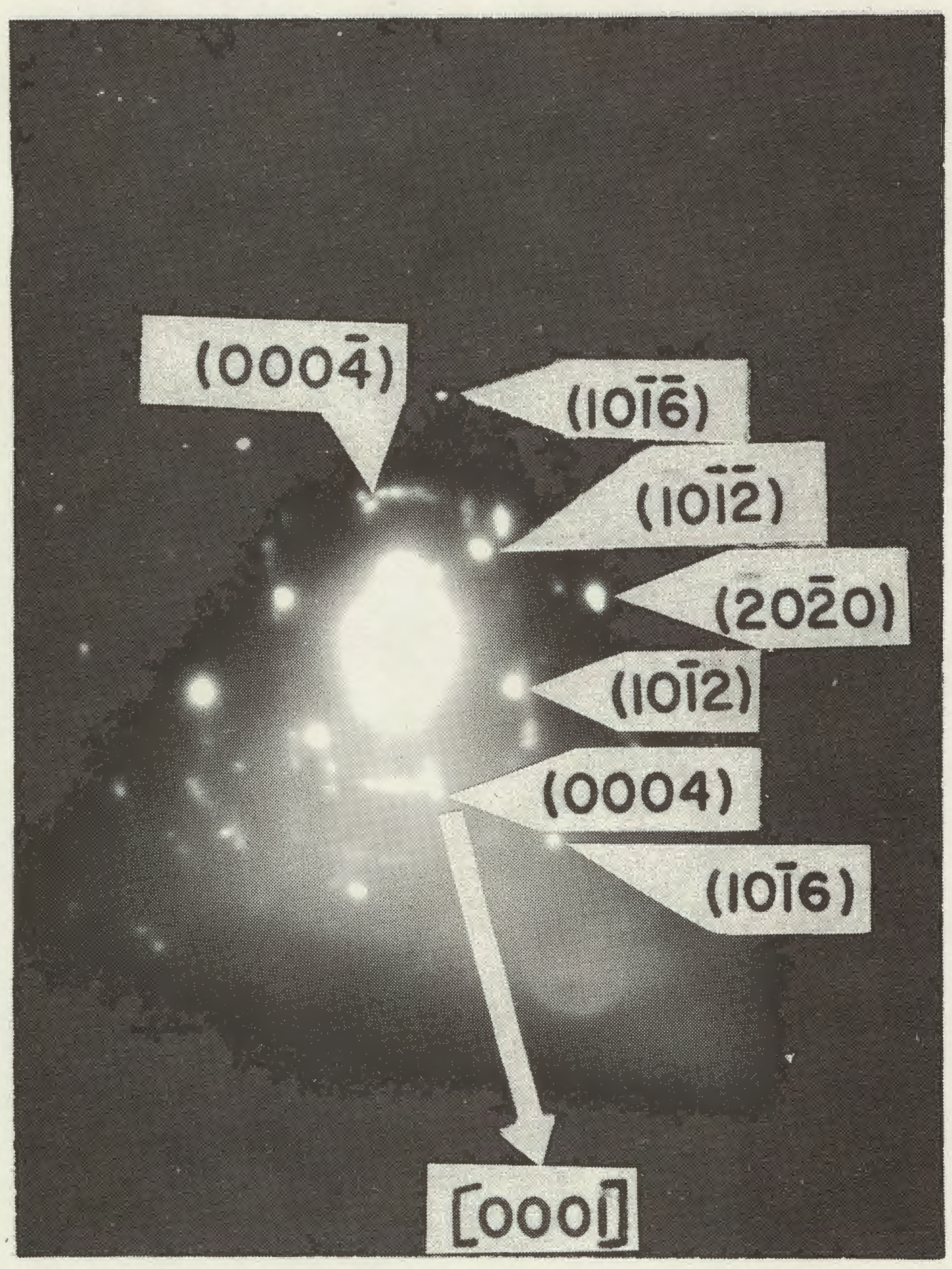

Figure 32 Electron diffraction pattern from growth facet on the graphite spheroid shown in Fig. 31. The [0001] direction is shown and can be related to Fig. 31 by clockwise rotation through 26 degrees.

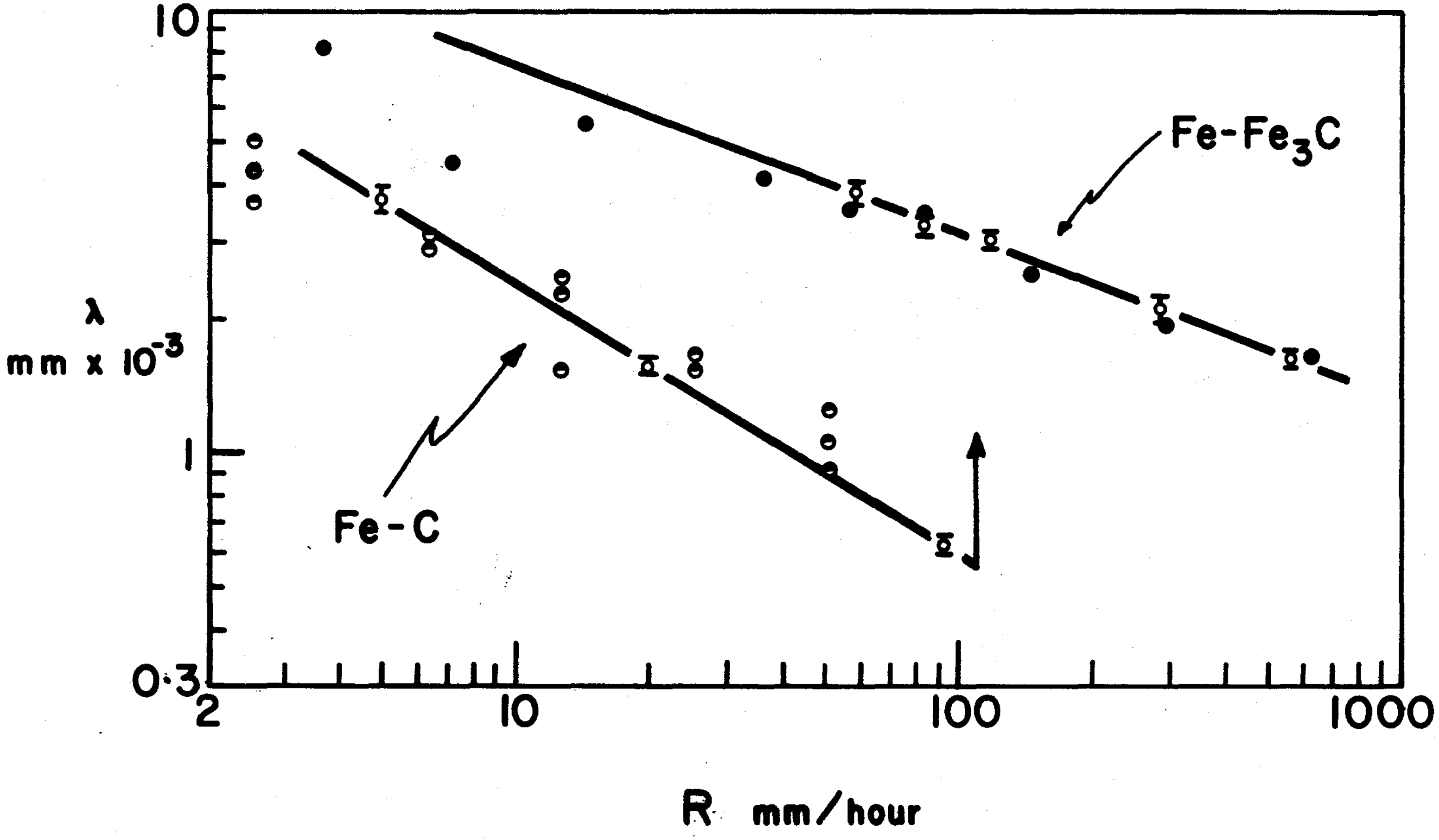

Figure 33 Plot of R vs λ for Fe-C and Fe-Fe$_3$C modes. Full circles after Wilkinson and Hellawell(26), half-full circles after Lakeland(37), and open circles from this investigation. The solidification rate of 110 mm/h at which the Fe-C mode transforms to the Fe-Fe$_3$C mode is shown.

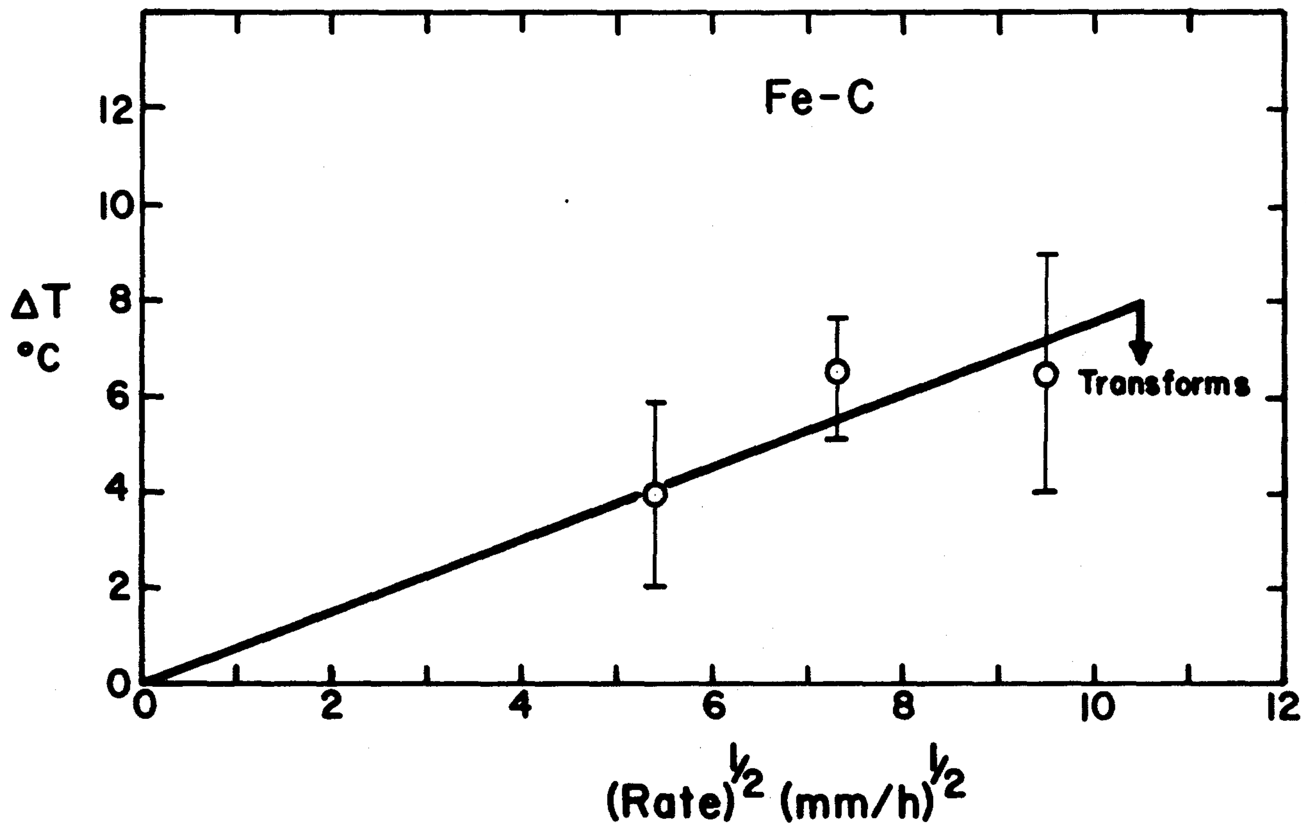

Figure 34 Plot of $R^{1/2}$ vs ΔT for the Fe-C mode.

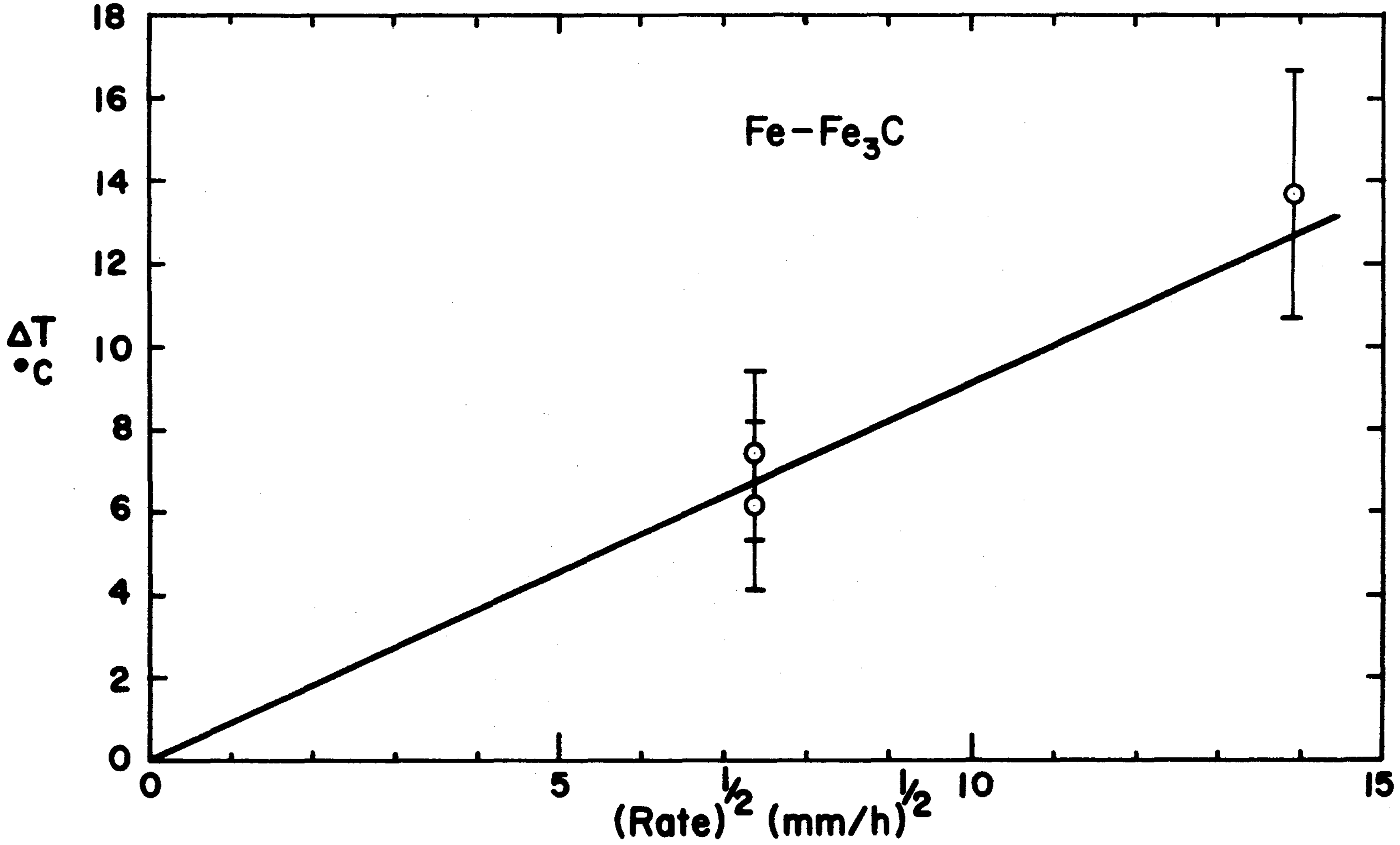

Figure 35 Plot of $R^{1/2}$ vs ΔT for the Fe-Fe$_3$C mode.

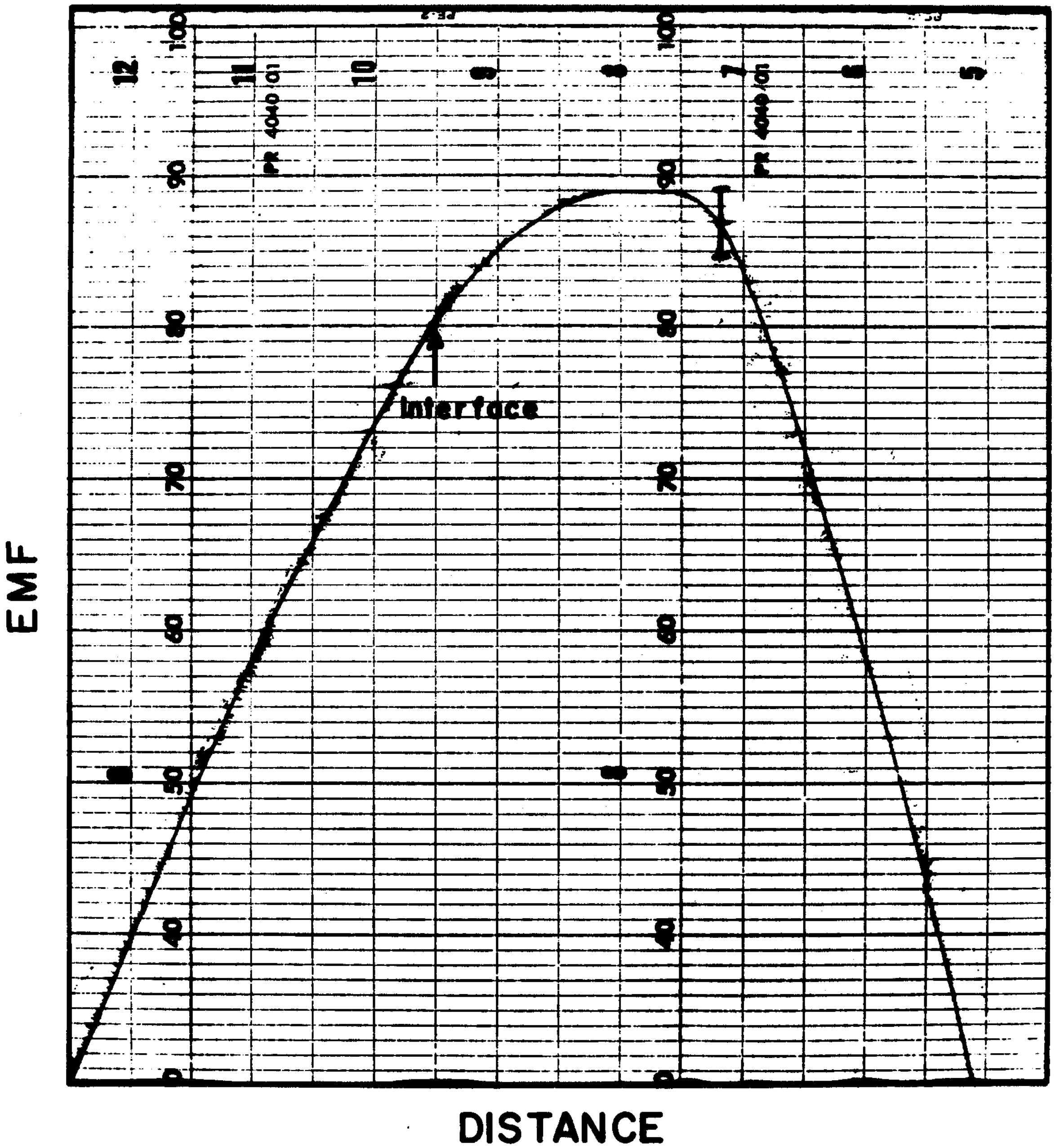

Figure 36 Reproduction of strip chart from which ΔT values were obtained. The estimated error in determining the temperature is indicated at the melting interface.

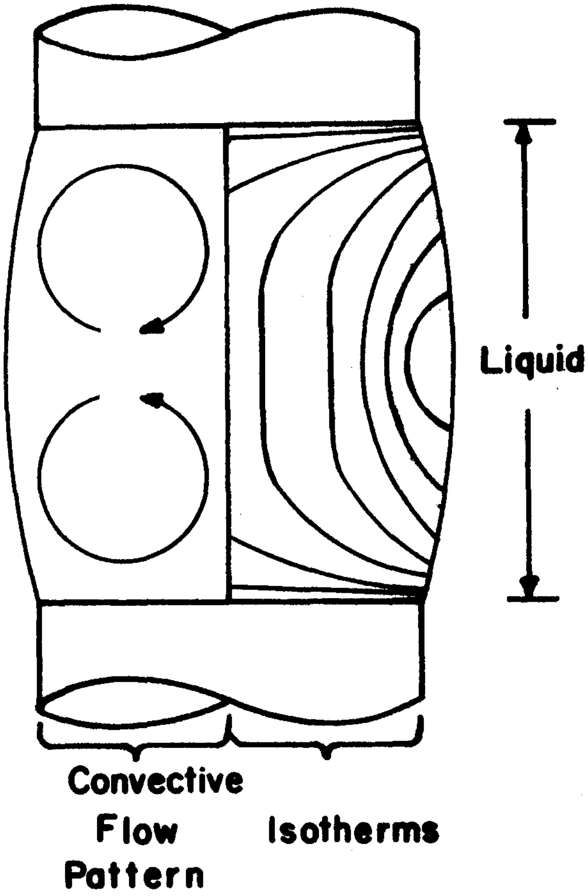

Figure 37   Isotherms and convective flow pattern in the molten zone.

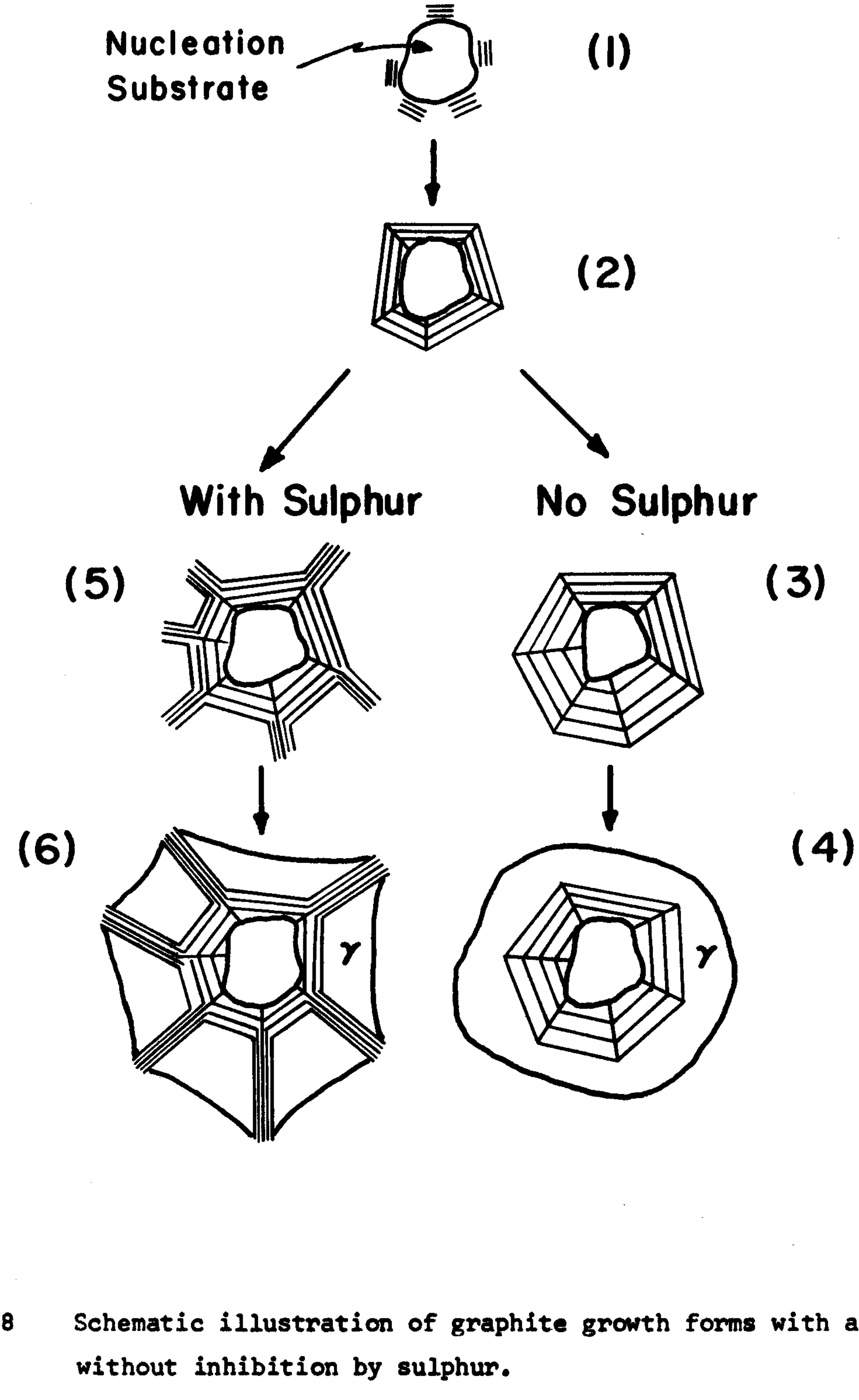

Figure 38 Schematic illustration of graphite growth forms with and without inhibition by sulphur.